Design and evaluation of a novel variable-length stepped scarf repair technique using a cohesive damage model

Mahdi Damghani [a,*], George Egerton [a], Gary A. Atkinson [a], Carwyn Ward [a], Adrian Murphy [b]

[a] School of Engineering, University of the West of England (UWE), Bristol, BS16 1QY, UK
[b] School of Mechanical and Aerospace Engineering, Queen's University Belfast (QUB), Belfast, BT9 5AG, UK

ARTICLE INFO

ABSTRACT

The advantages of Carbon Fibre Reinforced Polymers (CFRPs) are well established, but repairing CFRP components remains difficult and costly, posing challenges for industries like aerospace. This paper explores the design, modelling, inspection, and testing of a Variable Length Stepped Scarf (VLSS) repair scheme for highly loaded composite structures. A fully nonlinear 2D Finite Element Model (FEM) is used to design the VLSS repair, predict failure loads and modes, and model adhesive cohesion and delamination. The model incorporates a validated progressive damage model, general contact, and both force and geometric nonlinearities. Two manufacturing techniques involving hard repair patches and glass beads to maintain a constant bond line are employed. A 3D FEM validated against repaired composite coupons under uniaxial tension shows excellent agreement with experimental data. The static strength repair efficiency is approximately 80 % of a pristine sample, with failure displacements at 87 %, and Hooke's stiffness at 102 % of pristine laminates. Cohesive failure at adhesive overlap edges is identified as the cause of stiffness degradation, confirming experimental observations. This study contributes to both composite repair modelling and repair design optimisation.

1. Introduction

In recent decades, the use of Carbon Fibre Reinforced Polymers (CFRP) and Glass Fibre Reinforced Polymers (GFRP) has seen a significant increase across various industries, including aerospace, defence, marine, wind turbines, and oil and gas sectors. This surge in adoption is primarily due to their superior strength-to-weight (specific strength) and stiffness-to-weight (specific stiffness) ratios, improved corrosion resistance, and enhanced fatigue performance compared to traditional metals such as aluminum and titanium alloys. However, CFRP and GFRP are susceptible to damage from out-of-plane or transverse impacts. In aerospace, common sources of such impacts include debris during take-off and landing, bird strikes, lightning strikes, accidental tool drops during inspections, and collisions with ground equipment during taxiing [1,2]. For wind turbines, the leading edges of composite blades are vulnerable to impact damage from hailstones [3]. The severity of the impact damage can vary based on energy levels, causing delamination, debonding, fibre fracture, and matrix cracking. If the damage is extensive, particularly affecting load-bearing carbon or glass fibres, fibre replacement becomes necessary to restore the original load path of the structure [3]. Repairing damaged parts is essential as it is more cost-effective compared to replacing entire components.

The current aerospace industrial approach for repair of highly loaded CFRP laminated composite structures (primary structures such as wing, fuselage, rudder, tailplane, etc) is to provide a secondary load path by bolting a composite laminate patch, in the form of Single Lap Shear Joint (SLSJ) or Double Lap Shear Joint (DLSJ), on the damaged zone. However, these methods present several inefficiencies. The repaired surface is not flush, leading to aerodynamic discontinuities and increased fuel consumption. Additionally, bolted repairs result in high stress concentrations at the attachment points, with stresses reaching 2–3 times higher than those in metallic counterparts [4]. Moreover, such repairs involve additional weight from the metallic bolts (often titanium) and large repair patches that are not structurally optimised, further increasing the aircraft's overall weight. While these repairs can be quickly implemented, meeting tight financial constraints, especially given that aircraft grounding costs exceed £100,000 per day, such solutions are not optimal from a structural or aerodynamic perspective. In contrast, while adhesively bonded repairs offer potential advantages for composite materials - such as uniform load distribution, reduced stress concentrations, and lower weight - they cannot be certified for use in primary aircraft structures from an airworthiness perspective. This is

---

* Corresponding author.
E-mail address: mahdi.damghani@uwe.ac.uk (M. Damghani).

primarily due to the unreliability of bonded joints in aircraft construction, particularly when subjected to long-term environmental exposure, including moisture and temperature variations, which can degrade bond performance. Moreover, consistently achieving a perfect bond in repair applications remains a significant challenge, as even minor imperfections during the bonding process can lead to joint failure. As a result, bolted repairs continue to be the preferred method for primary structures despite their drawbacks, as they provide a more predictable, certifiable, and robust means of restoring structural integrity while minimising costly aircraft downtime.

Bonded composite structure repairs are generally categorised as ramped scarf [5] or stepped scarf [3] configurations (Fig. 1). Ramped scarf repairs require shallow scarf angles ($2° - 10°$) to recover the original static strength of the composite laminate, leading to extensive repair areas [5]. Such large areas pose challenges when repairing complex structures, like aircraft wings, due to interference with neighbouring elements (e.g., stringers and ribs), complicating design and implementation. To mitigate this, studies have explored optimising the scarf line geometry from straight to curved paths, reducing the repair size [6]. For more on these optimisations, see Ref. [6].

Stepped scarf repairs, when precisely designed for minimal repair area, can restore near-original static strength with minimal impact on the load path. Damghani et al. [3] introduced the Variable Length Stepped Scarf (VLSS) repair (Fig. 1b), which optimises the overlap lengths of individual plies, matching them to the parent material plies. This design facilitates effective load transfer and minimises repair size while restoring near-original static strength under tensile loading.

Extensive research has been conducted on the restored stiffness/strength, design parameters, failure behaviour, and modelling of composite scarf repairs. Ridha et al. [7] investigated the residual strength, damage progression, and ultimate failure of a bonded stepped scarf repair in composite panels. Their findings indicated that the Finite Element Model (FEM) combined with a material property degradation approach and a micromechanics-based failure criterion provided accurate predictions of the overall failure stress for both undamaged and damaged (with a hole) specimens. Notably, their numerical parametric studies demonstrated that the exponential traction-separation law was relatively insensitive to variations in adhesive strength, whereas models employing linear and trapezoidal laws were sensitive to both adhesive strength and toughness. This insight is significant for the reliable modelling of bonded composite repairs.

Bendemra et al. [8] investigated the influence of joint parameters on peak stresses in the adhesive bond-line for both ramped scarf and stepped scarf repairs using linear Finite Element Analysis (FEA). They examined six key joint design parameters: ply thickness, adhesive thickness, taper angle, stacking sequence, over-ply layup, and over-ply lap length. The study found that stepped scarf joints exhibited higher stress concentrations compared to ramped scarf joints, particularly at the ends of 0° plies. However, they also demonstrated that the introduction of over-plies and adjustments to joint design parameters could effectively mitigate stress peaks at the joint tips and step corners, improving the overall stress distribution in the repair.

Han et al. [9] employed static FEA, experimental studies, and continuum damage mechanics to investigate the tension failure mechanism in stepped scarf repairs of laminated composite structures. The authors utilised a mixed-mode fracture energy release rate criterion, based on the power law, to predict adhesive failure. Their results indicated that the load-deformation relationship remained linear up to the point of ultimate fracture. Additionally, experimental findings revealed that adhesive shear damage was the predominant mode of failure in the repaired specimens.

Psarras et al. [10] evaluated the efficiency of the stepped scarf repair technique using both dry and wet patch repair methods under tensile loading. They studied two types of repair patches - soft and hard - and compared two material removal techniques: conventional milling and laser ablation. Both methods successfully achieved the required geometry and dimensions. While milling was faster, laser ablation produced smoother surface finishes. The repair bond-line quality was assessed and found to be satisfactory, with both methods exhibiting low porosity. The laser/dry (hard patch) repair method yielded the highest recovery of strength and stiffness, followed by the milling/wet approach. Overall, 67% of the ultimate tensile strength and over 95% of the stiffness were restored, with the highest recovered strength (69%) observed in the laser/dry specimens.

Other researchers have explored the potential and efficiency of ramped scarf repairs in composite laminates. For example, Breitzman et al. [11] conducted an optimisation study of a composite ramped scarf repair patch under tensile loading. They utilised a circular repair patch with non-traditional ply orientations on a laminate featuring a 6° scarf angle. Multidimensional numerical optimisation was employed to
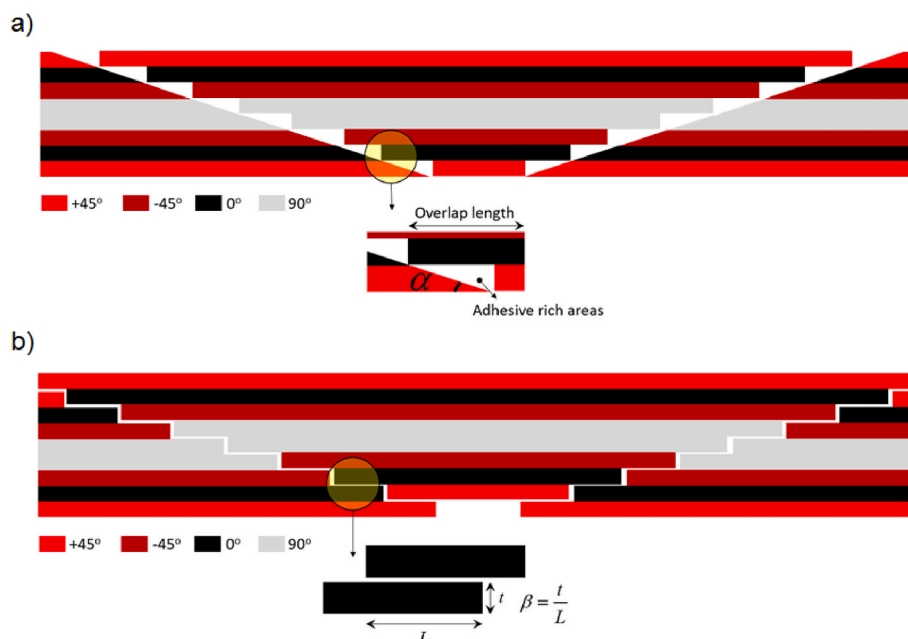
Fig. 1. Examples of laminated composite repair schemes, a) ramped scarf repair and b) stepped scarf repair as seen in the literature [3].

Table 1
Summary of repair types and their key findings in the literature.

Researcher	Repair Type	Research Procedure	Loading Type	Key Findings
Li et al. [15]	Stepped Scarf Repair	Experimental	Uniaxial Tensile	• The results identified the repair joint as the weakest failure point. • The results identified the repair joint as the weakest failure point.
Niedernhuber et al. [16]		Experimental	Uniaxial Tensile	• Fibre-oriented approach offers potential to reduce stepped repair geometries. • Achieved the same tensile strength with a 40 % shorter joint length in fibre-oriented joints compared to constant step-length joints. • Shorter step lengths between non-load-aligned UD plies did not significantly impact tensile strength.
Wang et al. [17]		Analytical	Uniaxial Tensile	• Adding steps and external plies could significantly enhance the load-carrying capacity of the repaired structure.
Masmanidis et al. [18]	Ramped Scarf Repair	Numerical	Uniaxial Tensile	• Joint strength is primarily governed by scarf angle, not adherend thickness. • Model robustness was validated through strength predictions compared with existing literature. • A simplified plane strain FE model proved efficient and was validated via full-scale repair tests. • Achieved a repair efficiency of 94 % relative to the intact laminate.
Ghazali et al. [19]		Experimental & Numerical	Compressive & Four-Point Bending	• Achieved 85% and 95% repair efficiency for scarf angle of 3° under compressive force and flexural loading, respectively.
Sun et al. [20]		Experimental & Numerical	Uniaxial Tensile	• Triangular CZM is ineffective for modelling ductile adhesives but suitable for brittle delamination. • 3D analysis showed non-uniform stress distribution, influenced by scarf angle and adherend layup. • Peel and shear stresses peaked at 0° plies, with shear stress higher and both increasing with scarf angle.

determine the optimal ply orientations that minimised von Mises stresses within the adhesive. Experimental results demonstrated a static strength restoration of 85% − 90%, illustrating the effectiveness of this repair method.

Pinto et al. [12] conducted a comprehensive study on the tensile behaviour of 3D scarf repairs in CFRP structures using a ductile adhesive. They applied 3D numerical optimisation with CZMs to simulate damage initiation and growth in the adhesive layer, using trapezoidal cohesive laws to account for adhesive ductility. However, their 3D finite FEM only incorporated stress-based failure criteria for composite plies and did not account for delamination in the repair plies. Their results showed exponential strength improvement with a reduction in scarf angle, suggesting that smaller scarf angles are always preferable. Additionally, they explored the effect of over-laminating plies on the outer and both faces of the repair to enhance efficiency. For repairs without over-laminates, repair efficiency was close to 50% of the undamaged laminate's strength for the smallest scarf angle. When over-laminating plies were used on both faces, efficiencies increased to approximately 70% of the undamaged strength. Maximum improvements in scarf repairs without over-laminates ranged between ∼ 30% and ∼ 60%, depending on the scarf angle.

Goh et al. [13] studied the strength of bonded composite scarf joints with varying bond-line flaw sizes through experimental testing, analytical modelling, and numerical simulation. Their experimental results demonstrated that the strength of a scarf joint with flaws depends on the ply angle adjacent to the crack tip and the flaw size. For both pristine and flawed scarf joints, the CZM accurately predicted the ultimate strength. The predictive model using CZM proved to be a reliable method for accounting for the effect of disbonding on the ultimate strength of scarf joints and repairs.

Table 1 provides a summary of the most relevant literature on both stepped and ramped scarf repair schemes. For a more comprehensive review of bonded repairs for aerospace composite structures, the reader is directed to Ref. [14].

In summary, carbon fibre reinforced composites can be repaired using either ramped or stepped scarf repair schemes. Literature indicates that the repair joint in both methods is the weakest point, with most repaired specimens failing at the joint due to shear failure of the adhesive. Although stiffness restoration of over 90% is commonly reported, no research to date demonstrates full 100% static strength restoration. Numerical simulations of repaired laminates are often conducted using finite element analysis (FEA), exploring various failure models for adhesives, including bilinear, trapezoidal, and exponential traction-separation laws. While all models show good correlation with experimental data, the exponential law is less sensitive to adhesive strength than the other two. Despite significant research, there is limited experimental and numerical data available on the VLSS repair scheme, as introduced by the authors.

This paper builds on previous work by the authors [3] and offers new insights through both numerical simulation and experimental validation of the VLSS repair scheme. A parametric numerical investigation is conducted using fully nonlinear 2D Finite Element Analysis (FEA) to design and optimise the VLSS repair scheme, with a focus on minimising size. The 2D FEA incorporates Cohesive Zone Modelling (CZM) for the adhesive layer and delamination in areas of high stress concentration, progressive failure analysis of the laminate, and accounts for both force and geometric nonlinearities.

Key novelties of the present work include.

- **VLSS repair design and optimisation**: Conducted using a fully nonlinear 2D FE-based study that incorporates CZM for adhesive and delamination, progressive failure of composite plies, and consideration of contact and geometric nonlinearities.
- **Enhanced manufacturing techniques**: Used to produce the VLSS repair, offering improvements over previous methods reported in Ref. [3].
- **Validation using 3D FEA**: Fully nonlinear 3D FEA is employed to compare and validate the experimental performance of the optimised VLSS repair.

This combined numerical and experimental approach offers improved understanding and optimisation of the VLSS repair scheme, which could significantly advance composite repair strategies.
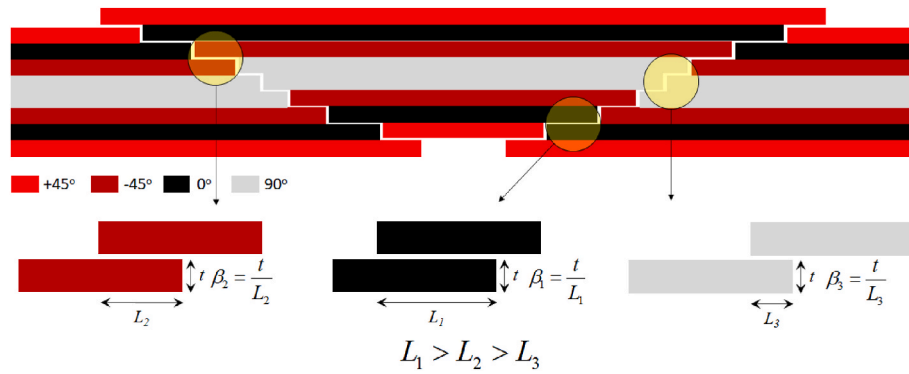
Fig. 2. A variable length stepped scarf repair (VLSS) [3].

2. Problem statement

The alternative to using a ramped scarf joint, as shown in Fig. 1a, is a variation of the stepped scarf repair scheme, known as the Variable Length Stepped Scarf (VLSS) repair, illustrated in Fig. 2. In the VLSS repair, the inevitable discontinuities in the fibres at the repair joint are mitigated by a series of lap joints that transfer the load via bonds from the fibres in a parent ply to those in an adjacent, overlapping repair ply [21,22]. A key principle of this repair method is that the material stiffness of the overlapping repair ply must match that of the underlying parent ply to ensure effective load transfer throughout the laminate stack.

The direct force normal to the joint and the shear force parallel to the joint in the parent ply determine the total force transferred through each lap joint in the stack. The total force in the ply dictates the necessary area of each lap, resulting in different lap areas as different plies carry varying loads. For instance, if the fibres in a unidirectional ply run tangential to the joint line (as shown by the grey ply in Fig. 2), minimal load will be transferred through the lap joint, allowing for a shorter lap length. Conversely, if the fibres lie normal to the joint line (the black ply in Fig. 2), a longer lap length is required to accommodate the higher load. By adjusting the lap lengths in this manner and eliminating the resin-rich sections typical of ramped scarf joints (Fig. 1a), the overall joint length is minimised, thus reducing the size of the repair.

In this paper, the authors present a first-of-its-kind optimisation study using validated, fully nonlinear 2D FEA to design a tailored VLSS repair. The primary objectives are to minimise the repair size while simultaneously restoring the original static strength of the structure. The optimised VLSS repair is then manufactured and subjected to experimental testing under uniaxial tensile load. Additionally, fully nonlinear 3D FEA is employed to provide a comprehensive interpretation of the experimental behaviour of the novel repair design.

3. Methodology

This section presents the mechanical properties of the materials used in this study (section 2). Details of 2D FEM (which is used for VLSS repair design) and 3D FEM (which is used for validation and understanding of experimental results) is provided in section 3.1. The design and sizing of VLSS repair using 2D FEM is covered in section 3.2. The manufacturing, quality control of the scarfed specimens and mechanical testing procedure are detailed in sections 3.3, 3.4 and 3.5, respectively.

3.1. Materials

The composite material used in this study is twill woven pre-impregnated carbon fibre ($AX - 5180$). The carbon prepregs consist of 54% fibre by volume (60% by weight) embedded in epoxy resins with Chemical Abstract Service (CAS) numbers $25036 - 25 - 3$ (⟨20% < by

Table 2
Mechanical properties of woven CFRP (AX-5180) fabric plies [23].

Mechanical properties	Units	AX-5180 CFRP
$E_{11} = E_{22}$ (elastic modulus in 1 & 2 directions)	MPa	67094
G_{12} (shear modulus in plane 1–2)	MPa	4831
S_t (tensile strength)	MPa	620
S_c (compressive strength)	MPa	403
S_S (shear strength)	MPa	87
Strain to failure	Strain	0.01
ϑ_{12} (Poisson's ratio)	N/A	0.04
t_{ply} (cured ply thickness)	mm	0.22

weight), $28064 - 14 - 4$ (⟨20% < by weight) and proprietary co-polymers (⟨20% < by weight). The mechanical properties of the CFRP are given in Table 2. The adhesive used is $XA120$ $150g$ film with minimum and maximum cure temperatures of $80°C$ and $120°C$, respectively. The mechanical properties for the adhesive are given in Table 3.

3.2. Finite element analysis (FEA)

Two types of Finite Element Models (FEM) were employed in this study. A 2D FEM was utilised for a parametric study and to design the repair for minimum size and optimal strength recovery (see section 3.2.1). In contrast, a 3D FEM was used to analyse the behavior of the optimised repair from the 2D studies and to provide detailed validation against experimental results. Both 2D and 3D FEMs employed quasi-static analysis using the ABAQUS/Explicit solver. The choice of ABAQUS/Explicit was based on the following considerations.

    I. Greater ease in handling complex contact problems compared to implicit analysis.

    II. Lower computational resource requirements compared to implicit analysis.

    III. Compatibility with the user-defined material model described in section 3.2.3, which is only applicable in explicit analysis.

3.2.1. 2D Finite Element Model (2D FEM)

The present study employs a 2D plane-stress numerical analysis of a tensile-loaded VLSS repair joint, based on a stepped scarf repair scheme,

Table 3
Mechanical properties of adhesive film XA120 [3].

Mechanical properties	Units	XA120
E (modulus of elasticity)	MPa	1644
G (shear modulus)	MPa	610
S_t (tensile strength)	MPa	30
S_S (shear strength)	MPa	35
ϑ_{12} (Poisson's ratio)	N/A	0.35
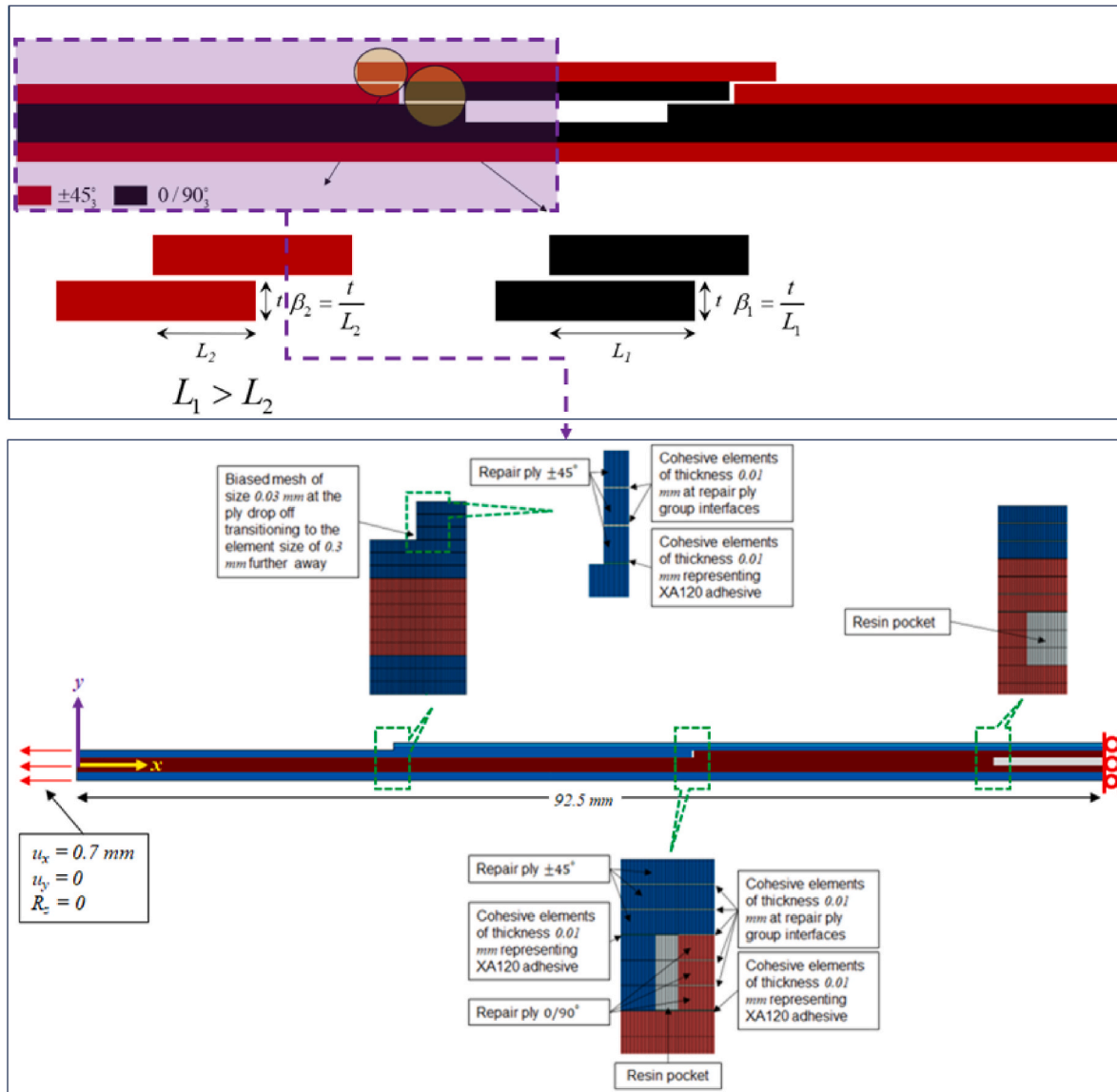
Fig. 3. Geometry, boundary conditions and 2D meshing of the repaired specimens (shown for $\beta_1 = \beta_2 = 1/40$).

Table 4

Cohesive interface mechanical properties.

Material	K_n (MPa)	$K_s = K_t$ (MPa)	t_n^0 (MPa)	$t_s^0 = t_t^0$ (MPa)	$G_n^C \left(\dfrac{J}{m^2}\right)$	$G_s^C = G_t^C \left(\dfrac{J}{m^2}\right)$
XA120 [a] adhesive	164400	61000	30	35	300	700
Epoxy resin for Axiom pre-preg [b]	380000	142000	70	110	453	1860

[a] Taken from [3,30,31].

[b] Interpolated from [33–35].

for the design and optimisation of the repair (as detailed in section 3.3). The laminate is symmetric about its mid-plane with a balanced stacking sequence, i.e. $[\pm 45_3/0_3]_S$, and applies the concept of ply groups (clustering of plies with similar orientations). Since both the geometry and loading of the problem are symmetric, and to enhance computational efficiency, only half of the model is used for design, analysis, and optimisation. In other words, half of the overall gauge length of the repaired specimens ($0.5 \times 185\ mm = 92.5\ mm$) is modelled in the FEM, as shown in Fig. 3.

The right end of the structure is roller-clamped, allowing displacements only in the y direction. Conversely, the left end of the structure has an imposed displacement in the x direction, while displacements and rotations in the y direction and about the z axis are fully restricted. Based on a mesh size study conducted in earlier work by the authors [3] on the same repair geometry and loading as the current study, an element size of $0.3\ mm$ was found to provide reasonable accuracy. However, due to the presence of cohesive elements, a biased meshing strategy was adopted. At the ply drop-off locations, where stress concentrations are critical, the element size was reduced to $0.03\ mm$, transitioning to $0.3\ mm$ further away from these locations. It is worth noting that Woo [24] suggests that, in the presence of cohesive elements, the finite element size should be selected with consideration for the cohesive zone size. He proposes that the size of the cohesive zone can be approximated as

$$l_{cz} = M \frac{EG_c}{\tau_0^2} \qquad (1)$$

where E, G_c and τ_0 denote the material Young's modulus, fracture energy and maximum interfacial strength, respectively, while M is a constant between 0 and 1. Based on [25], parameter M is often unity or close to unity. The cohesive element size is then approximated as [25]

$$l_e \leq \frac{l_{cz}}{N_e} \qquad (2)$$

where N_e is the number of elements in the cohesive zone. A minimum of three elements are required within the cohesive zone to ensure accurate results. Hence, considering the values given in Tables 3 and 4, the chosen element size of $0.03\ mm$ is a sufficiently fine mesh and falls within the range proposed by Refs. [24–26].

The carbon plies are modelled using linear, reduced-integration, plane stress elements (CPS4R) [27]. CPS4R elements have a single integration point (as opposed to the standard four integration points) located at the centroid of the element to improve computational efficiency while maintaining reasonable accuracy, given the mesh refinement used in the FEM (see Fig. 4). The plane stress elements have four nodes, each with two displacement degrees of freedom (DOF), totalling eight DOFs per element. In contrast, the adhesive layer and the interface between the repair plies are modelled using 2D cohesive elements (COH2D4). These cohesive elements are four-node elements with two integration points through the thickness (see Fig. 4).

The cohesive elements in the adhesive layer are designed to simulate debonding failure at the adhesive interface, whereas those between the repair plies are intended to predict the initiation and propagation of delamination. Notably, no cohesive elements are used at the interfaces of the parent plies to reduce computational costs for the repair design,

analysis, and optimisation. This modelling simplification is justified by the findings of [3], which demonstrated that delamination occurred and progressed within the repair plies without causing damage to the parent plies.

3.2.2. 3D Finite Element Model (3D FEM)

The present study employs a 3D numerical analysis of the smallest optimised repair design obtained from the 2D FEM outlined in section 3.2.1. This 3D FEM is utilised for a detailed behavioural analysis of the optimised repair and serves as a validation against the experimental results.

A full-length 3D model ($185\ mm$) is used for analysis. The left end of the structure is fully clamped, restricting displacements in all directions, while the right end has an imposed displacement of $3\ mm$ in the x direction. Displacements in the y and z directions and rotations about the z-axis are fully constrained. Based on the mesh study by Ref. [3], a solid element size of $0.3\ mm$ is selected for accurate results (Fig. 5).

A detailed mesh sensitivity study was conducted to determine the appropriate cohesive element size, considering four options: $1.00\ mm$, $0.5\ mm$, $0.35\ mm$ and $0.2\ mm$. The failure load of the optimised 3D FEM was plotted against these cohesive element sizes (see Figure A1 in the appendix). Results showed that for cohesive element sizes of $0.35\ mm$ or smaller, the predicted failure load remained stable. Therefore, a cohesive element size of $0.35\ mm$ was adopted for this study.

The carbon plies are modelled using eight-node quadrilateral general-purpose continuum shell elements with reduced integration and hourglass control (SC8R), as shown in Fig. 6. The adhesive layer and interfaces between the repair plies are modelled using 3D cohesive elements (COH3D8). These elements have eight nodes with four integration points through the mid-thickness. Due to the finer mesh used on the repair side (including repair plies and cohesive elements representing delamination and debonding), TIE constraints are applied. These constraints bond the surfaces of the bulk material mesh (SC8R) to the corresponding top and bottom cohesive surfaces (COH3D8), allowing for differing mesh densities.

3.2.3. Material model

Considering the bi-directional nature of the twill materials used in this study, a constitutive material model for fabric-reinforced composites was adopted from the literature [23,28]. This model was implemented via a built-in VUMAT user subroutine in ABAQUS/Explicit. It is

CPS4R linear, reduced integration, plane stress element with single integration point at the centroid of the element

COH2D4 cohesive elements with two integration points in the thickness direction (blue crosses)
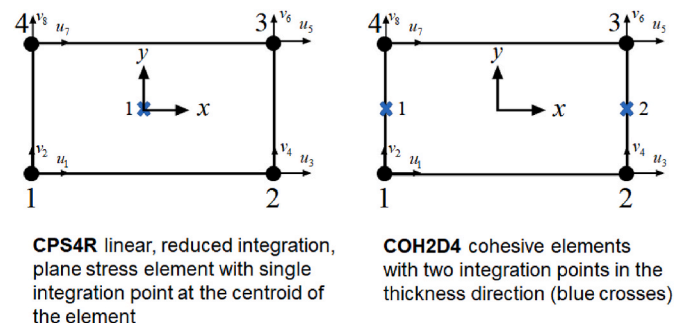
Fig. 4. Schematic illustration of 2D cohesive (COH2D4) and plane stress (CPS4R) elements.
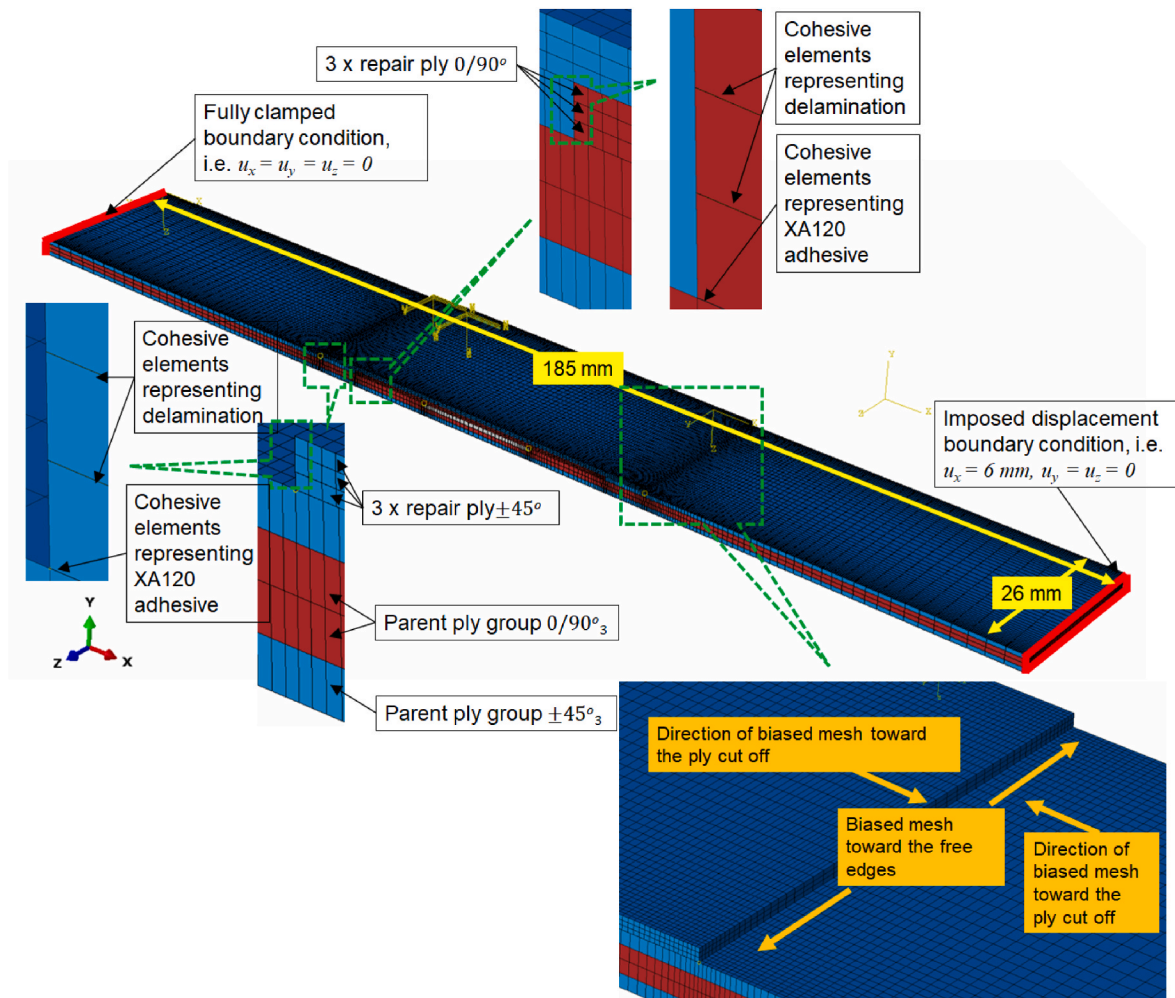
Fig. 5. Geometry, boundary conditions and 3D meshing of the repaired specimens (shown for $\beta_1 = \frac{1}{20}$, $\beta_2 = \frac{1}{10}$, see Fig. 6 for graphical definition of β_1 and β_2).

essential to note that the material model was applied using plane stress elements for the 2D FEMs and continuum shell elements for the 3D FEM. The use of continuum shell elements in 3D FEM ensures a more accurate representation of the stress state, allowing for consideration of both in-plane and out-of-plane stresses in the failure model.

The material model incorporates progressive stiffness degradation due to fibre damage, matrix cracking, and plastic deformation under loading. It considers two primary failure mechanisms: fibre-dominated failure in tension or compression along the two fibre directions and matrix-dominated failure under in-plane shear. Given that the complete material characterization of AX5180 and the corresponding failure processes are elaborated in Ref. [23], only a concise overview of the material model is presented in the subsequent sections.

3.2.3.1. Elastic stress-strain relationship. The material elastic stress-strain relations, in local coordinate system, is given as

$$
\begin{bmatrix} \varepsilon_{11} \\ \varepsilon_{22} \\ \varepsilon_{12}^{el} \end{bmatrix} = \begin{bmatrix} \dfrac{1}{(1-d_1)E_1} & \dfrac{-\upsilon_{12}}{E_1} & 0 \\ \dfrac{-\upsilon_{21}}{E_2} & \dfrac{1}{(1-d_2)E_2} & 0 \\ 0 & 0 & \dfrac{1}{(1-d_{12})2G_{12}} \end{bmatrix} \begin{bmatrix} \sigma_{11} \\ \sigma_{22} \\ \sigma_{12} \end{bmatrix} \tag{3}
$$

where E_1 and E_2 are Young's moduli in the 1 (fibre direction) and 2 (perpendicular to the fibre direction) directions, G_{12} is the in-plane shear modulus in $1-2$ plane, and υ_{12} is the Poisson's ratio in $1-2$ plane. d_1 ($0 \le d_1 \le 1$) and d_2 ($0 \le d_2 \le 1$) are damage variables which are associated to fibre fracture along the ply 1 and 2 directions, respectively. d_{12} ($0 \le d_{12} \le 1$) represents micro-cracking of the matrix.

3.2.3.2. Fibre response. The fibre damage variables use damage elasticity and effective stresses as

$$
\begin{aligned}
d_{1+} &= d_{1+}(\overline{\sigma_{1+}}) \\
d_{1-} &= d_{1-}(\overline{\sigma_{1-}}) \\
d_{2+} &= d_{2+}(\overline{\sigma_{2+}}) \\
d_{2-} &= d_{2-}(\overline{\sigma_{2-}})
\end{aligned} \tag{4}
$$

where d_{1+} and d_{1-} are the tensile and compressive damages along the fibre in the ply direction 1, respectively. d_{2+} and d_{2-} are the tensile and compressive damages along the fibre in the ply direction 2, respectively. Upon damage initiation, the updated stress state is used to calculate effective stresses

$$
\overline{\sigma_{1+}} = \frac{\sigma_{11}}{1-d_{1+}}
$$

$$
\overline{\sigma_{1-}} = \frac{-\sigma_{11}}{1-d_{1-}}
$$

$$
\overline{\sigma_{2+}} = \frac{\sigma_{22}}{1-d_{2+}} \tag{5}
$$

$$
\overline{\sigma_{2-}} = \frac{-\sigma_{22}}{1-d_{2-}}
$$

Throughout the analysis, the elastic domain is defined via the damage activation functions (F_i)

$$
F_i = \phi_i - r_i \le 0
$$

$$
\phi_i = \frac{\overline{\sigma_i}}{X_i}; (i = 1+, 1-, 2+, 2-) \tag{6}
$$

where X_i is the tensile ($+$) and compressive ($-$) strength for uniaxial loading along the fibre directions 1 and 2. The damage thresholds (r_i) are initially set to one. After damage activation ($\phi_i = 1$), the damage thresholds at any given time (t) increase based on

$$
r_i(t) = \max \phi_i(t^*); t^* \le t \tag{7}
$$

The evolution of damage variables is a function of the damage

thresholds (r_i), the elastic energy density per unit volume at the point of damage initiation (g_0^i), the fracture energy per unit area under uniaxial tensile/compressive loading (G_f^i), and the characteristic length of the FE mesh (L_c). The damage variables are formulated as

$$
d_i = 1 - \frac{1}{r_i} e^{\left(-\frac{2g_0^i L_c}{G_f^i - g_0^i L_c}(r_i - 1) \right)} \tag{8}
$$

where L_c is the square root of the area ($\sqrt{A}$) and cube root of volume ($\sqrt[3]{V}$) of the largest element in the model for 2D and 3D elements, respectively. The elastic energy density per unit volume at the point of damage initiation is given as

$$
g_0^i = \frac{X_i^2}{2E_i} \tag{9}
$$

Besides, $G_f^i \approx L_{\max} E_f^i$ where $L_{\max}$ is the maximum element length to avoid over prediction of energy dissipation. E_f^i is the input energy per unit volume of the uniaxial tensile/compressive coupons up to the point of failure obtained from experimental testing of [23].

3.2.3.3. Shear response. To simulate the shear response of the material, it is assumed that the shear behaviour and the mechanism of ply in-plane shear degradation are mainly determined by the matrix [29] not the fibre. Thus, to characterise the overall matrix behaviour, elastic, plastic, nonlinear and the damage response of the matrix are considered and discussed below.

3.2.3.3.1. Elastic behaviour. The elastic shear response of the matrix as a function of effective stresses is defined as

$$
\overline{\sigma_{12}} = \frac{\sigma_{12}}{1-d_{12}} = 2G_{12}\varepsilon_{12}^{el} = 2G_{12}\left(\varepsilon_{12} - \varepsilon_{12}^{pl} \right) \tag{10}
$$

where ε_{12}, ε_{12}^{el} and ε_{12}^{pl} are total, elastic, and plastic strains, respectively.

3.2.3.3.2. Plastic behaviour. The state of plasticity is defined by the value of the elastic domain function (F) as

$$
F = |\overline{\sigma_{12}}| - \overline{\sigma_{y0}} - C\left(\varepsilon^{pl} \right)^p \tag{11}
$$

where $\overline{\sigma_{y0}}$ is the initial effective shear yield stress and C and p are experimental material parameters [23]. $F < 0$ corresponds to stress states inside the elastic domain where the material endures elastic damage. However, $F = 0$ represents the plastic deformations.

3.2.3.3.3. Damage. The state of damage is defined by the damage activation function (F_{12}) as

$$
F_{12} = \phi_{12} - r_{12} \le 0
$$

$$
\phi_{12} = \frac{\overline{\sigma_{12}}}{S} \tag{12}
$$

The function ϕ_{12} is the criteria for shear damage initiation of the matrix. S is the shear strength of the ply. The damage is a non-decreasing

CS8R linear, reduced integration, continuum shell element with single integration point at the centroid of the element

COH3D8 cohesive elements with four integration points in the thickness direction (blue crosses)
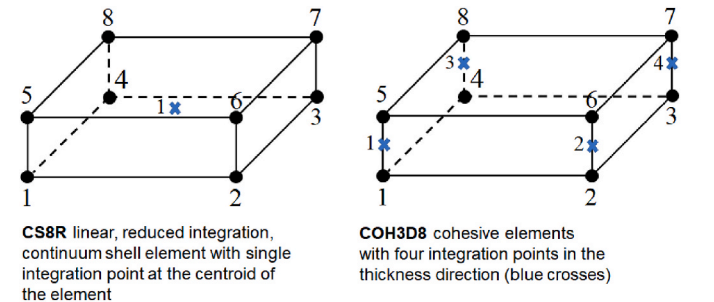
Fig. 6. Schematic illustration of 3D cohesive (COH3D*) and plane stress (CS8R) elements.
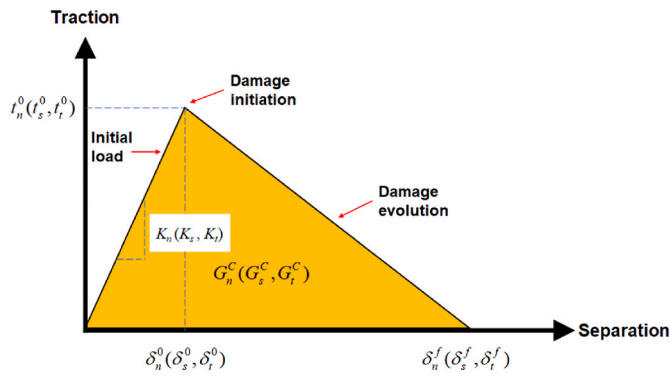
Fig. 7. Bi-linear traction-separation law.

value. Thus, it must be monotonically increasing when damage takes place. After damage activation ($\phi_i = 1$), the damage thresholds (r_{12}) at any given time (t) increase according to

$$r_{12}(t) = \max \phi_{12}(t^*); t^* \leq t \tag{13}$$

It is further assumed that d_{12} increases as a logarithm of r_{12} until a maximum value of $d_{12}^{\max}$ is reached. Hence

$$d_{12} = \min\left(\alpha_{12} \, \mathrm{Ln}(r_{12}), d_{12}^{\max}\right) \tag{14}$$

α_{12} is a constant and in this study $\alpha_{12} = 0\ 0.38$ [23]. $d_{12}^{\max}$ is the maximum shear damage and in this study $d_{12}^{\max} = 0.67$ [23].

3.2.4. Modelling the adhesive layer

The constitutive behaviour of the cohesive layers is defined using a mixed-mode traction-separation law, where each mode follows a bi-linear traction-separation relationship (see Fig. 7). This approach has demonstrated good agreement with experimental results [23]. Damage initiation is modelled using a quadratic nominal stress interaction function, where damage occurs when the sum of the nominal stress ratios equals one. This criterion can be expressed as

$$\left(\frac{\langle t_n \rangle}{t_n^0}\right)^2 + \left(\frac{t_s}{t_s^0}\right)^2 + \left(\frac{t_t}{t_t^0}\right)^2 = 1 \tag{15}$$

where $\langle t_n \rangle$, t_s and t_t are the existing normal, first and second shear stresses, respectively.

Note that the Macaulay bracket function, $\langle t_n \rangle = (|t_n| + t_n)/2$, is used. Here, t_n^0, t_s^0 and t_t^0 denote the peak values of nominal stress when deformation occurs purely in the normal direction or in the first or second shear direction, respectively. Once damage initiation occurs, damage progression is defined by the rate of material stiffness degradation, triggered when the corresponding initiation criterion is satisfied. The damage evolution is governed by the following law

$$\left(\frac{G_n}{G_n^C}\right) + \left(\frac{G_s}{G_s^C}\right) + \left(\frac{G_t}{G_t^C}\right) = 1 \tag{16}$$

where G_n, G_s and G_t are the existing energy release rates in normal, first and second shear modes, respectively. G_n^C, G_s^C and G_t^C denote the critical total energy release rates (fracture energies) for the corresponding modes. Essentially, these critical fracture energies correspond to the area under the triangular representation shown in Fig. 7.

Cohesive interface parameters for adhesive and delamination modelling are presented in Table 4. The damage initiation stresses for the XA120 adhesive, sourced from Refs. [30,31], are conservatively reduced based on tensile testing of the adhesive bulk material [3] and initiation stress values from Ref. [32], to account for the manufacturing process employed in this study.

The stiffness of cohesive elements is determined using the ratio of the normal modulus (E) and shear modulus (G) to the thickness ($t = 0.01\ mm$). Specifically, E values for XA120 and epoxy resin are 1644 MPa and 3800 MPa, respectively, while G values are 610 MPa and 1420 MPa, respectively.

$$K_n = \frac{E}{t}$$

$$K_s = K_t = \frac{G}{t} \tag{17}$$

where K_n is the normal stiffness, and K_s and K_t are the shear stiffnesses in directions 1 and 2, respectively.

3.2.5. Other nonlinearities

Throughout the analysis for both 2D and 3D FEMs, a general contact algorithm is utilised to prevent the penetration of failed elements into

Table 5
Summary of designs used in the parametric study.

Repair design $\beta_1 - \beta_2$	Repair design ID	Numerical failure load (kN)	Numerical failure mode
Intact (pristine)	0	27.690	Fibre fracture
1/15-1/15	1	19.968	Cohesive failure
1/20-1/5	2	20.072	Cohesive failure
1/20-1/10	3	21.060	Cohesive failure and fibre fracture
1/20-1/20	4	20.124	Fibre fracture
1/25-1/25	5	16.553	Fibre fracture
1/30-1/30	6	16.830	Fibre fracture
1/35-1/35	7	17.108	Fibre fracture
1/40-1/40	8	19.365	Fibre fracture
1/45-1/45	9	19.032	Fibre fracture
1/50-1/50	10	19.266	Fibre fracture
1/55-1/55	11	19.370	Fibre fracture
1/60-1/60	12	18.902	Fibre fracture
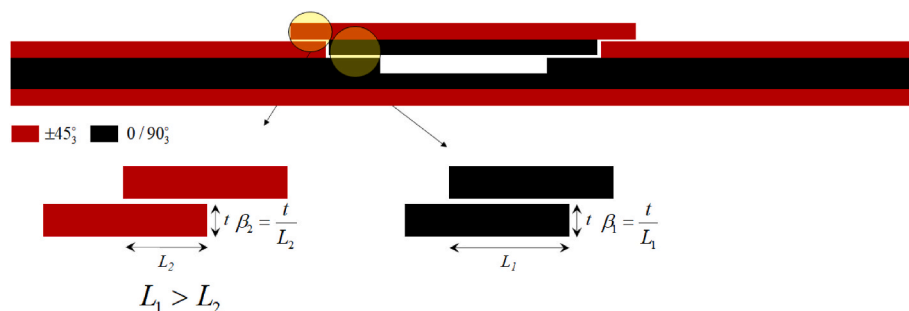
Fig. 8. Schematic illustration of Variable Length Stepped Scarf (VLSS) repair design for the parametric study.
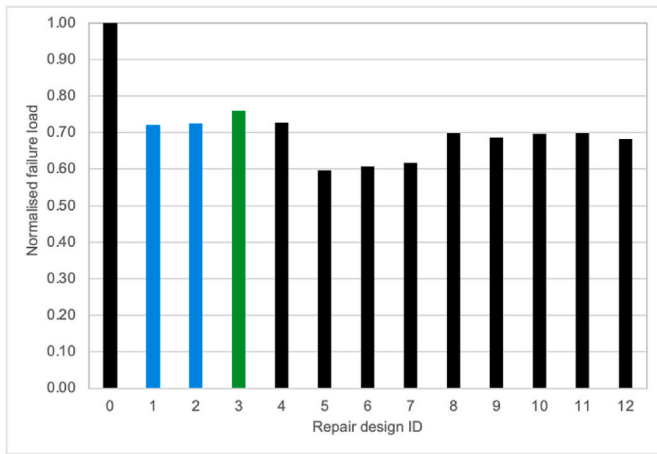
Fig. 9. Normalised numerical failure load of repair designs compared to the numerical failure load of the intact laminate (Black, blue and green bars show fibre fracture, cohesive failure and combined cohesive/fibre fracture failure modes, respectively).

the surrounding intact material. This element-based surface contact, automatically defined by the ABAQUS/Explicit solver, encompasses all bodies within the model. Additionally, force nonlinearity (follower load), large deformations, and geometric nonlinearity are accounted for in the analysis.

3.2.6. Load application

The tensile load in both 2D and 3D FEMs was applied as an imposed displacement using the SMOOTH STEP load amplitude function in ABAQUS/Explicit. This function utilizes a fifth-order polynomial to apply the load gradually, minimising significant energy variations at the start and end of the loading phase.

3.2.7. Mass scaling

Due to the presence of cohesive elements and the inherently small-time steps (on the order of 10^{-9} s) required for this analysis, mass scaling was implemented to accelerate solution time without affecting the loading rate. Sensitivity studies were conducted for various mass scaling factors of 10, 100, 1000 and 10000. It was determined that a factor of 1000 increased the time step to 10^{-8} s while keeping the kinetic energy below 5% of the internal energy throughout the analysis. Therefore, a mass scaling factor of 1000 was selected for both the 2D and 3D FEMs.

3.3. Repair design and optimisation

The ideal repair, in the form of stepped scarf repair (as shown in Fig. 1b), is one that minimises its size by reducing the overlap lengths L_1 and L_2 (as illustrated in Fig. 8) while ensuring failure occurs through one of the following modes:

- Fibre fracture within the parent plies.
- Simultaneous fibre fracture of both parent and repair plies.

Although some cohesive failure within the adhesive bond is inevitable, it is essential that the repair patch remains attached to the structure and continues to function as a load-bearing element, thereby preserving overall structural integrity.

To achieve such an ideal repair, a parametric study is conducted in which the design variables L_1 and L_2 are continuously adjusted. Initially,

a repair of maximum size ($\beta_1 = \beta_2 = 1/60$) is considered, as this configuration demonstrated the characteristics of an ideal repair in a previous study [3]. The design variables are then simultaneously and continuously reduced in increments of 5 mm. A nonlinear analysis, accounting for both material and geometric nonlinearities, is performed. At the end of each analysis, the failure modes and forces are evaluated.

The smallest repair configuration demonstrating ideal characteristics is further refined by incrementally reducing the overlap length L_2 of the less load-bearing ply groups $\pm45_3^\circ$ in steps of 5 mm. This fine-tuning process minimises the repair size while maintaining its optimal structural performance.

Table 5 summarises the numerical failure modes and loads for all design candidates.

Fig. 9 presents the failure load of each repair design, normalised to the numerical failure load of the intact laminate. The figure indicates that repair design 3 achieves the highest failure load and demonstrates the most desirable failure mode compared to the other designs. An ideal failure mechanism in repaired composites involves simultaneous fibre fracture in both the repair and parent laminates. However, achieving this often necessitates large repairs with long overlaps to adequately diffuse shear stresses along an extended adhesive bond-line. To optimise repair design, it is crucial to allow for very localised cohesive failures that do not propagate along the bond-line, while still promoting simultaneous fibre fracture in both the repair and parent plies. This approach ensures efficient load transfer and maintains structural integrity without excessively increasing the repair size.

Fig. 10 illustrates the damage progression in 2D FEA for design ID 3, which exhibits the ideal failure mode: fibre fracture without detachment of the repair patch before laminate failure. This configuration achieves the highest numerical failure load. Initially, damage develops in the adhesive at the overlap interface of the 0_3 plies (Fig. 10b) when the load reaches $f = 788.00$ N per unit width. As the load increases to $f = 800.80$ N, a second damage site appears in the adhesive at the overlap interface of the $\pm45_3$ plies. These damage formations reduce the stiffness of the repaired laminate, leading to a subsequent load drop in the following time steps.

At $f = 551.60$ N, widespread cohesive damage occurs (Fig. 10e), though it does not extend across the full adhesive length. Ultimately, the laminate fails due to cohesive damage, predominantly at the $\pm45_3$ plies, and fibre fracture across all plies (Fig. 10f). This progression validates the ideal failure mode, where localised cohesive damage allows the repair patch to remain attached, effectively transferring load until fibre fracture occurs.

3.4. Manufacture of pristine and repair specimens

Three pristine rectangular 120 mm × 280 mm laminated plates with quasi-isotropic stacking sequence of $[\pm45_3, 0_3]_s$ are hand laid using twill woven pre-impregnated carbon fibre (AX-5180) plies. The laminates are cured in a heated press at $120°C$ temperature for 70 minutes under 100 psi pressure.

One of the cured pristine laminates is used to cut four pristine test coupons, each 26 mm wide and 280 mm long. The remaining two laminates are used for scarfing and repair manufacture, as designed and analysed in section 3.2.5.

The scarfing is carried out using a Computer Numerical Control (CNC) milling machine. The laminates are machined with a Bridgeport 600 vertical milling centre, using a 10 mm, 4-flute tungsten end mill at a feed rate of 100 mm/min and a spindle speed of 7500 rpm. Cutter paths for each sample profile are programmed using FeatureCAM software, enabling a faster milling path with a 0.2 mm depth of cut per pass until the required scarfing profile is achieved.
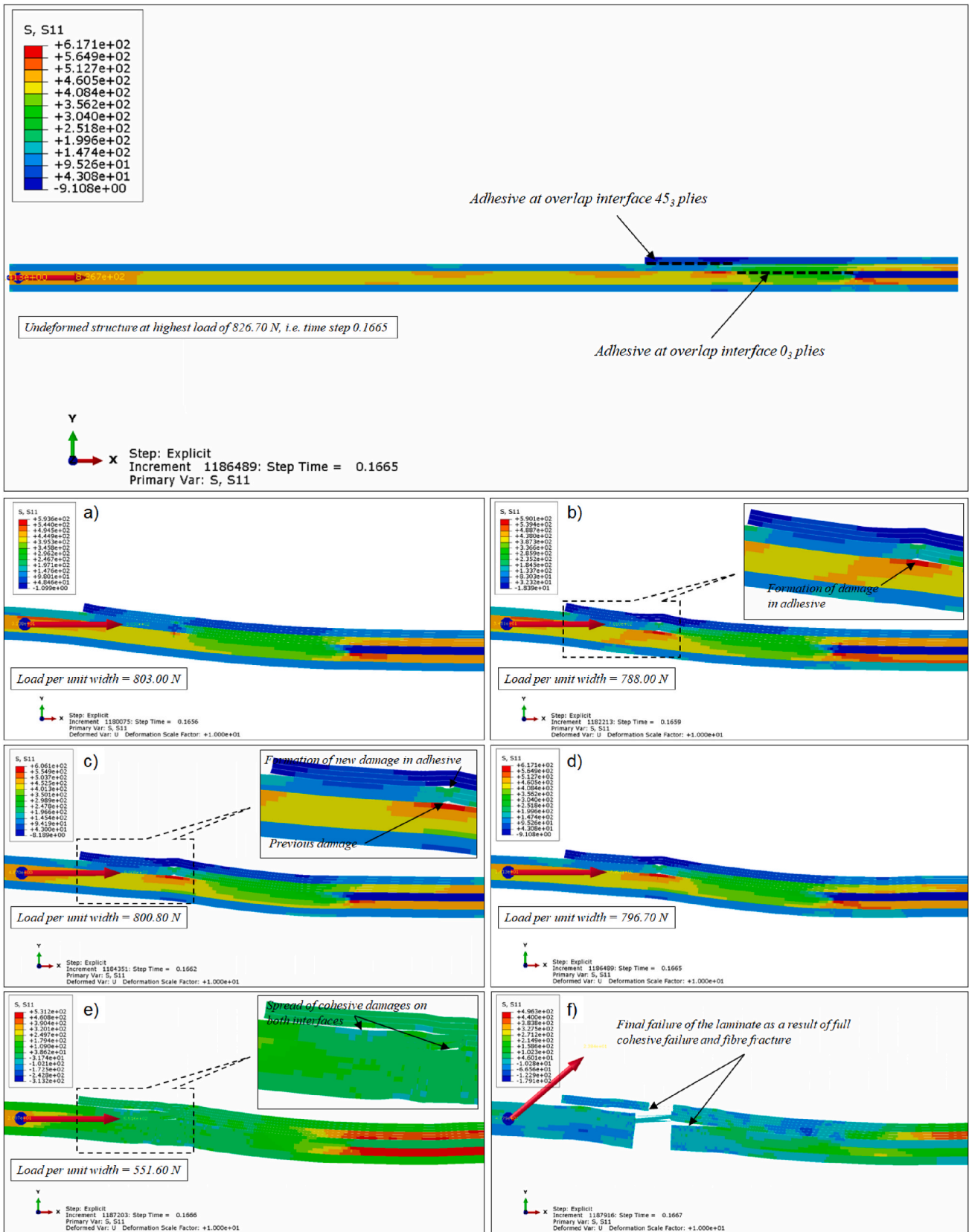
Fig. 10. Sequence of damage mechanisms of the smallest repair (design ID 3) for various time steps (t) and load per unit width (f); a) $t = 0.1656\,s$, $f = 803.00\,N$, b) $t = 0.1659\,s$, $f = 788.00\,N$, c) $t = 0.1662\,s$, $f = 800.80\,N$, d) $t = 0.1665\,s$, $f = 796.70\,N$, e) $t = 0.1666\,s$, $f = 551.60\,N$ and f) $t = 0.1667\,s$ (Deformation is scaled x10 and the contour plots show stresses in x direction in units of MPa).
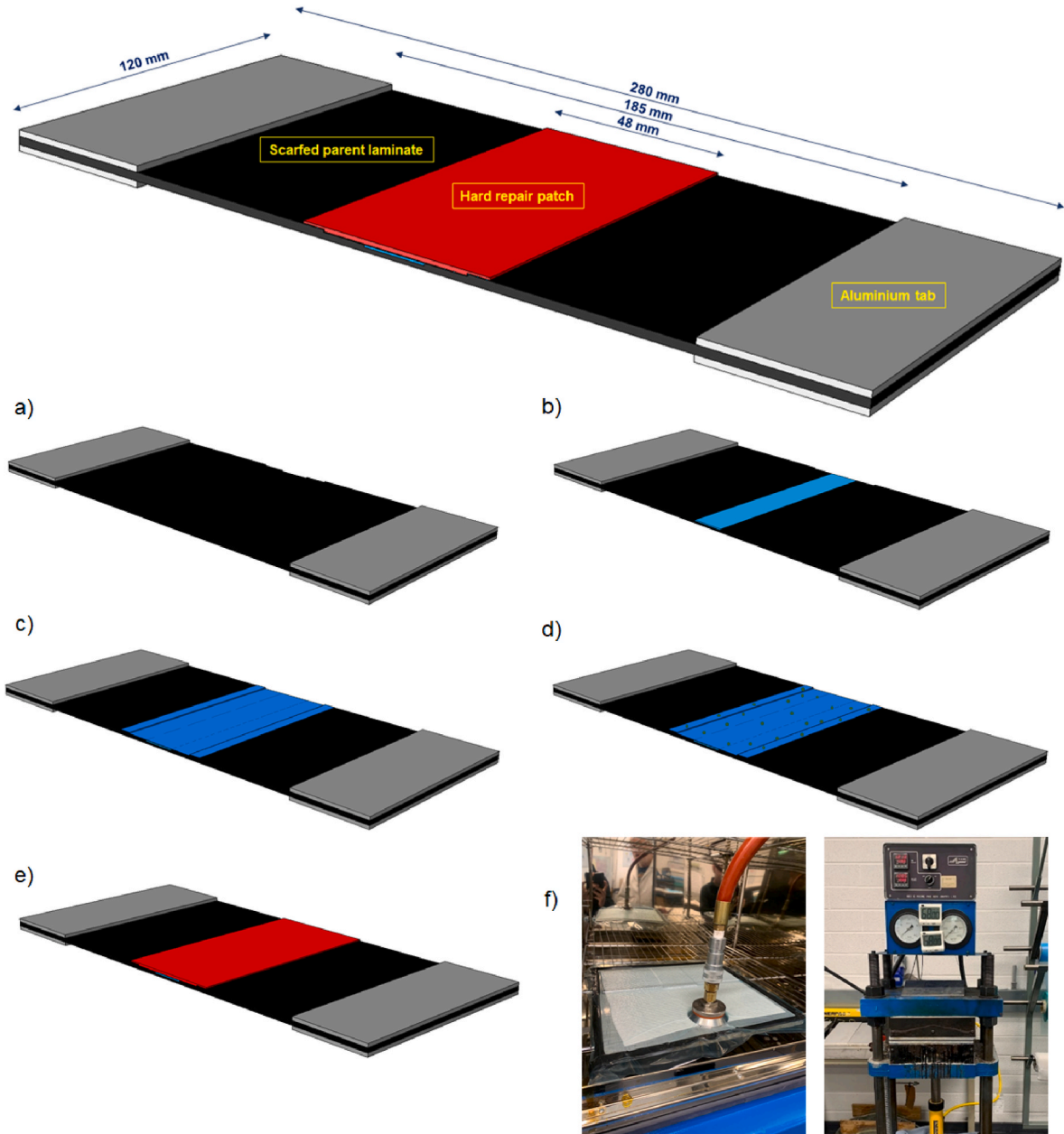
Fig. 11. Illustration of sequence of repair manufacture activities, a) scarfed laminate, b) filling the damage pocket with resin, c) application of XA120 adhesive film, d) application of glass beads having diameter of 0.2 *mm*, e) application of hard repair patch, f) vacuum bagging (left) and pressing (right) the repair in heated press.
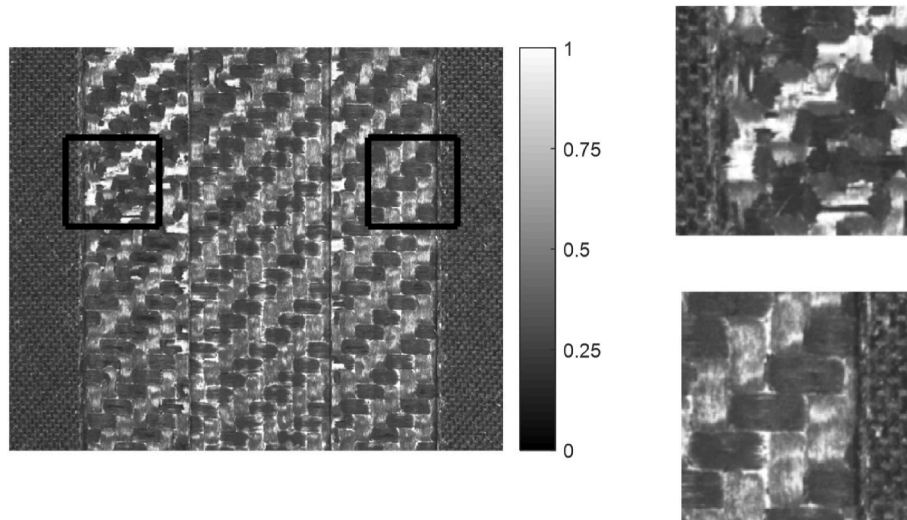
Fig. 12. Standard greyscale image of a portion of the scarf before cutting into coupons. The images to the right are closeups of the two highlighted regions with the upper image less precisely milled than the lower.
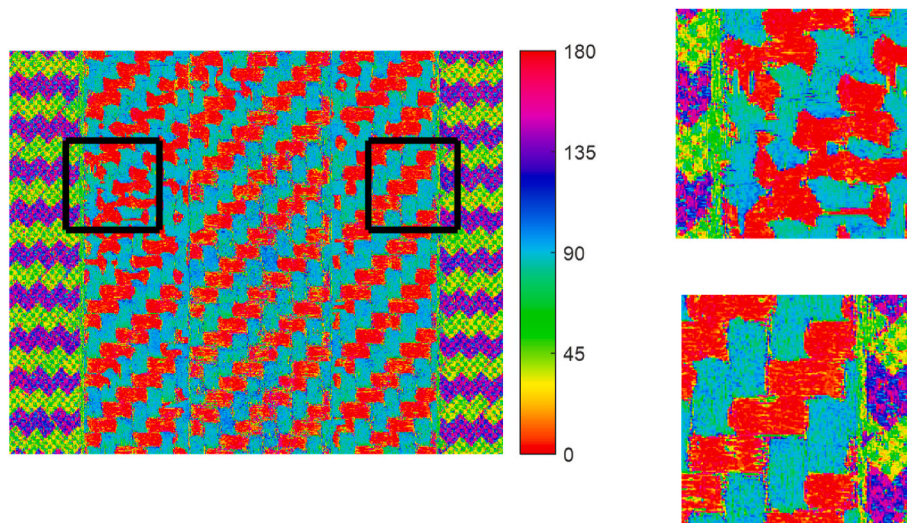
Fig. 13. Angle of linear polarisation image corresponding to Fig. 12, representing estimated fibre angles for each pixel of the image.

Two repair patches, each $120\,mm$ wide and $48\,mm$ long, with a stacking sequence of $[\pm45_3, 0_3]$, are manually laid and cured using the heated press, like the pristine laminates. The patches are then cut to size using the CNC milling machine. This type of patch is referred to as a "hard repair patch" as it is cured prior to application.

The two scarfed laminates are lightly sanded using 120 grit sanding mesh. The bonding surfaces are initially washed with distilled water, dried, and cleaned with alcohol. The damage void is filled with resin (Fig. 11b). Next, XA120 adhesive film is cut to size and applied to the prepared surfaces (Fig. 11c). Glass beads with a diameter $0.2\,mm$ are spread on the surface to maintain a constant bond line thickness of $0.2\,mm$ (Fig. 11d). A minimal amount of glass beads is used (less than $0.5\,\%$ of the combined adhesive and glass beads mass) to avoid altering the adhesive's mechanical properties [36].

The repaired laminate is then placed in a vacuum bag and cured in a heated press set to $120°C$ for $1\,hour$, followed by an additional hour of post-curing. It is important to note that for the first repair laminate (Repair A), no additional pressure is applied by the heated press, resulting in a pressure of $14.7\,psi$. Conversely, in the second repair laminate (Repair B), the heated press applies an additional $15.3\,psi$, totalling $30\,psi$ of combined pressure. This extra pressure is introduced to enhance the bonding process, creating a stronger bond without forcing the molten adhesive to escape from the bond line while maintaining a consistent thickness of $0.2\,mm$ due to the presence of glass
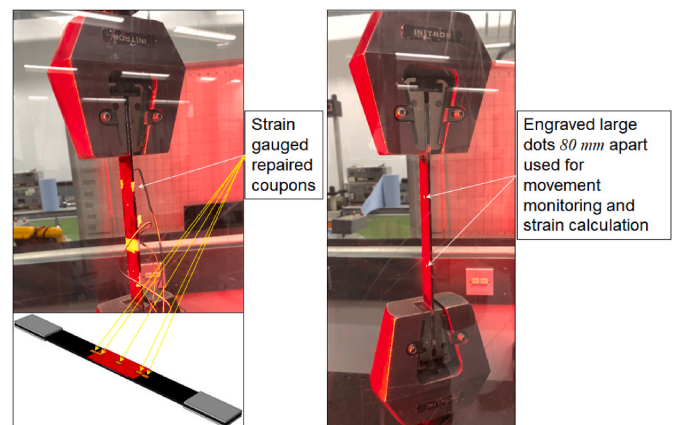
Fig. 14. Illustration of strain gauged repaired coupons (left) and AVE2 non-contacting video extensometer set-up of pristine coupons (right).
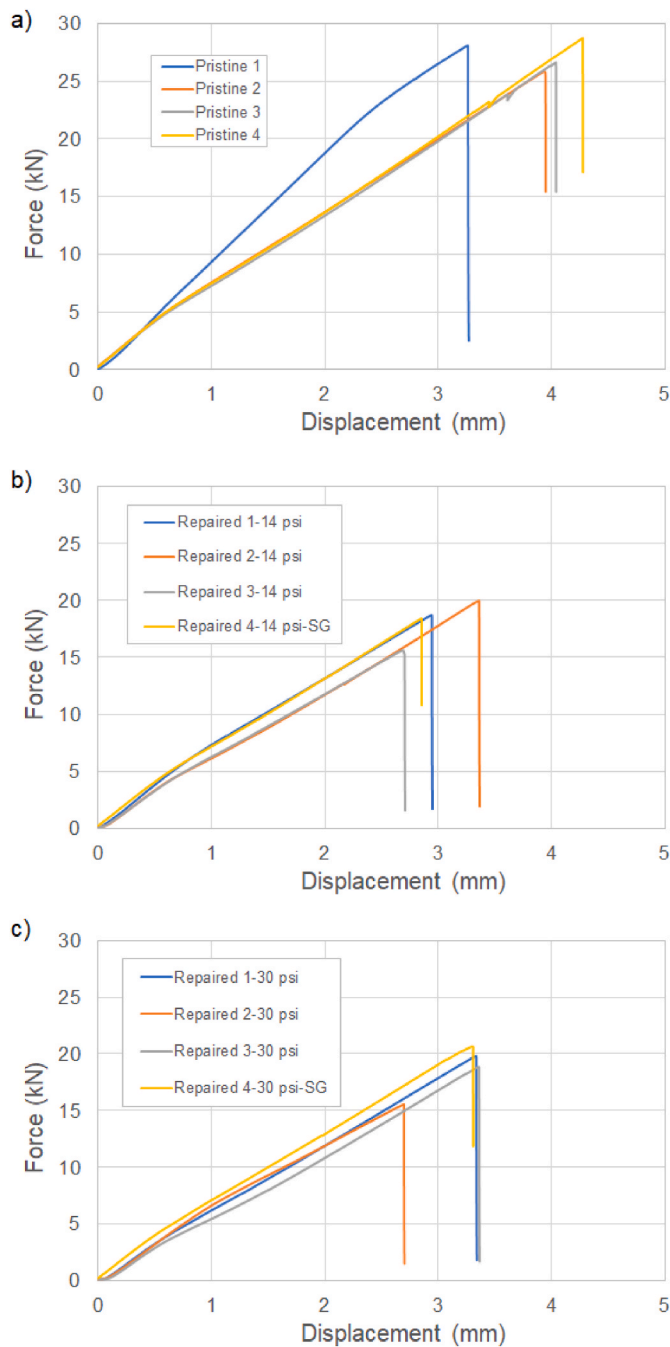
Fig. 15. Force-displacement graphs of a) pristine, b) repair A and c) repair B.

beads.

Pristine, repair A, and repair B laminates are cut into four tensile strip coupons, each 26 mm wide, for mechanical testing.

3.5. Machine vision and scarfing quality check

The precise removal of material for a scarf repair is challenging due to the thin interfaces between layers. This difficulty applies not only to components with complex geometries but also to simpler planar components, as used in this study. The numerical calculations in this paper assume a perfect scarfing process. To qualitatively evaluate the validity of this assumption for the physical samples, we employ the polarisation inspection method described in Ref. [37].

Fig. 12 shows a greyscale image of a section of the scarf area, highlighting two regions with differing levels of quality. In the right-hand region, the underlying layer of a $(0/90)$ ply is clearly visible, whereas in the left-hand region, it is not. However, due to the limitations of this standard image, it is challenging to examine the details of the scarf imperfections.

In Fig. 13, the fibre angle for each pixel in the image has been estimated using the polarisation technique described in Ref. [37]. The right-hand region displays a clean pattern, indicating minimal disruption to the underlying layer. However, it should be noted that this does not entirely rule out the possibility of a small portion of that layer being inadvertently removed. In the left-hand region, while the scarfing is indeed imperfect as predicted from the standard image, the pattern remains sufficiently like the $(0/90)$ ply orientation to cause minimal impact on the overall repair. Evaluating the numerical effects of such scarf imperfections will be the focus of future work. It is worth mentioning that, in previous work [3], this level of scarfing imperfection had little impact (only 1%) on the overall strength and stiffness of the repaired laminate and was therefore deemed acceptable for the present study.

The remaining regions of the scarf, not included in the figures above, were all comparable to those shown and have therefore been omitted from the paper for brevity.

3.6. Mechanical testing

To have statistically repeatable data, three coupons for each repair design are tested in tension using a 100 kN capacity INSTRON tensile machine at a speed of 2 mm/min. One of the coupons for each repair design is strain gauged at 5 locations as shown in Fig. 14, i.e. just before and after the bond-line and in the middle of the repair. The strain gauges have grid resistance of $120.0 \pm 0.3\% \, \Omega$. The size of the strain gauges is chosen so that they cover an area larger than the CFRP weave size thereby enabling appropriate averaging of strain data. The strains in the pristine coupons are measured using an INSTRON AVE2 Non-contacting Video Extensometer by measuring the movement of two white dots at 80 mm apart positioned in the middle of the specimens (see Fig. 14 (right)). This strain measuring technique allows the measurement of strains throughout the test up to the point of failure without the need to pause the test for removing a physical extensometer providing more accurate and representative results. The positioning of strain gauges is to observe the flow of strain path from the parent laminate (closer to the loaded end) to the repair patch and back to the parent laminate (closer to the fixed end).

4. Results and discussions

This section presents results from both the experimental procedure (section 4.1) and the 3D numerical simulation (section 4.2).
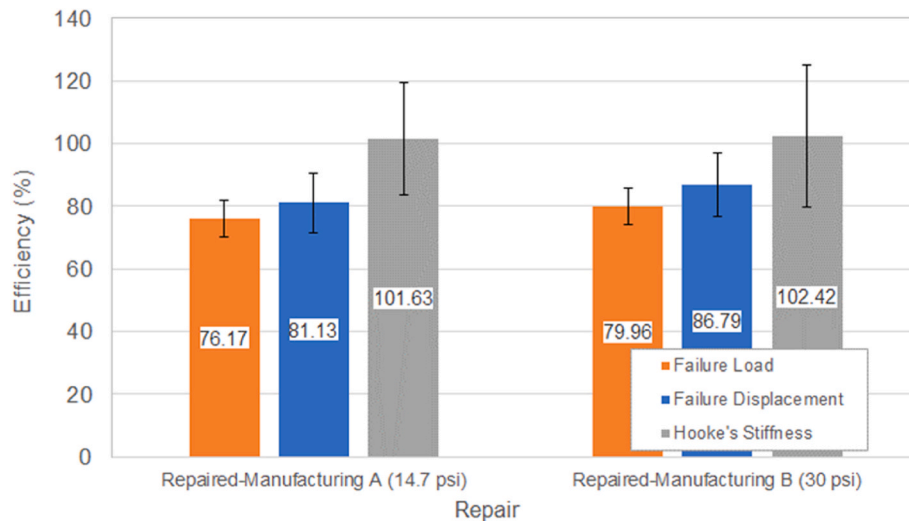
Fig. 16. The efficiency of repaired laminates, i.e. failure load, failure displacement and Hooke's stiffness, normalised to the pristine values for both manufacturing types A and B. The percentage ratio of the standard deviation to the mean values for each case is represented as bars ($100 \times SD/Mean$).

Table 6
Summary of experimental failure load, failure displacement and Hooke's stiffness of both pristine and repaired coupons.

Pristine Laminates			
Specimen ID	Failure Load (kN)	Failure Displacement (mm)	Hooke's Stiffness (N/mm)
Pristine 1	28.11	3.56	7892.62
Pristine 2	25.87	3.95	6549.83
Pristine 3	23.88	3.61	6606.14
Pristine 4	23.78	3.54	6725.22
Average	25.41	3.67	6943.45
SD [a]	2.04	0.19	636.99
Average $\pm$ SD	25.41 $\pm$ 2.04	3.67 $\pm$ 0.19	6943.45 $\pm$ 636.99
Repaired Laminates-Manufacturing Method A [b]			
Repaired 1	20.76	2.95	7817.80
Repaired 2	19.63	3.37	5727.37
Repaired 3	18.84	2.71	8404.83
Repaired 4	18.18	2.86	6277.36
Average	19.35	2.97	7056.84
SD	1.11	0.28	1261.12
Average $\pm$ SD	19.35 $\pm$ 1.11	2.97 $\pm$ 0.28	7056.84 $\pm$ 1261.12
Repaired Laminates-Manufacturing Method B [c]			
Repaired 1	21.54	3.34	6998.66
Repaired 2	19.86	2.70	9388.55
Repaired 3	18.93	3.37	5645.49
Repaired 4	20.94	3.31	6412.42
Average	20.32	3.18	7111.28
SD	1.16	0.32	1616.13
Average $\pm$ SD	20.32 $\pm$ 1.16	3.18 $\pm$ 0.32	7111.28 $\pm$ 1616.13

[a] Standard deviation (SD).
[b] Using 14.7 psi pressure on the repair patch.
[c] Using 30 psi pressure on the repair patch.

4.1. Experimental results

The experimental results are organised into three sections: force-displacement response (section 4.1.1), stress-strain response (section 4.1.2), and failure mode (section 4.1.3) of the test specimens.

4.1.1. Force-displacement response

Force-displacement graphs of pristine, repair A and repair B coupons are shown in Fig. 15. The behaviour of both the pristine and repaired laminates is nearly linear, with a sudden, abrupt failure characteristic of

CFRP laminated composite structures, as also observed by Han et al. [9]. A kink at approximately 0.6 *mm* displacement is present in all test coupons, including the pristine ones, which is attributed to test set-up characteristics, such as fixture compliance and the settling of end fixtures during loading.

Failure load, displacement at failure, and Hooke's stiffness for repairs using manufacturing methods A (Repair A) and B (Repair B) are normalised to the corresponding values of the pristine coupons and are illustrated in Fig. 16. Additionally, a summary of the extracted data from the load-displacement graphs is provided in Table 6.

As shown in Fig. 16, Repairs A and B, on average, restore 76.16% and 79.96% of the pristine coupons' static strength, respectively. Compared to the similar repair design in study [3], the improved manufacturing technique in the current study, i.e. using hard patch repair and glass beads, resulted in a significant $\approx$ 14% enhancement in static strength restoration. Additionally, the application of extra curing pressure in Repair B led to a 3.8% increase in static strength restoration.

Displacements at failure for Repairs A and B were 81.13% and 86.79% of the pristine coupons, respectively. This reduction is mainly due to the combined effects of reduced load-bearing capacity and load eccentricity, which cause rotation at the repair-parent interface and limit higher in-plane displacements in the repaired specimens. Like the failure load, the displacement at failure for Repair B shows a 5.66% improvement over Repair A, highlighting the positive impact of increased curing pressure on overall repair performance.

For clarity and statistical context, the percentage ratio of the standard deviation to the mean values for each measured parameter is depicted as bars in Fig. 16. The length of each standard deviation bar represents $100 \times SD/Mean$.

Hooke's stiffness is approximated as the ratio of failure load to the displacement at failure. Interestingly, both repairs exhibit a slight improvement in stiffness compared to the pristine coupons, with increases of 1.63% and 2.42% for Repairs A and B, respectively. This can be attributed to the fact that the coupons predominantly function in the axial direction. Thus, their axial stiffness can be approximated as EA/L, where E is the homogenised modulus of elasticity in the loading direction, A is the cross-sectional area, and L is the gauge length of the specimens. In the repaired coupons, A is increased compared to the pristine coupons, while L remains unchanged and E is minimally affected. This results in a higher EA/L ratio for the repaired coupons, leading to greater experimental Hooke's stiffness.

Additionally, as shown in Table 6, the pristine coupons exhibit a lower standard deviation for both displacement at failure and Hooke's
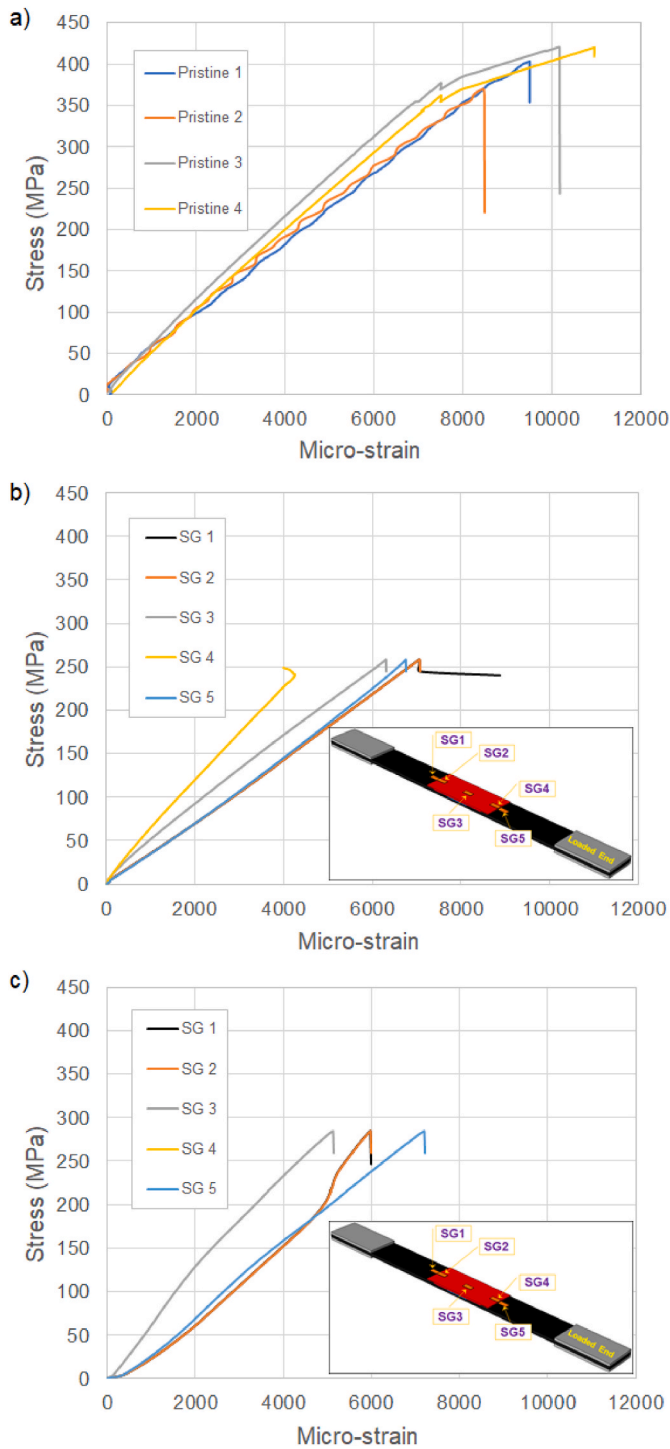
Fig. 17. Stress-strain graphs of a) pristine, b) repair A and c) repair B.

Table 7
Summary of experimental failure stress, average failure strain and homogenised Young's modulus of both pristine and repaired coupons.

Pristine Laminates			
Specimen ID	Failure Stress (MPa)	Average Failure Strain (μstrain) [a]	Membrane Homogenised Young's Modulus
Pristine 1	403.23	9507.00	42300.00
Pristine 2	370.13	8492.00	43500.00
Pristine 3	377.20	7514.00	50300.00
Pristine 4	370.85	8048.00	48100.00
Average	380.35	8390.25	46050.00
SD	15.58	845.07	3778.45
Average ± SD	380.35 ± 15.58	8390.25 ± 845.07	46050 ± 3778.45
Repaired Laminates-Manufacturing Method A			
Repaired 1	298.14	6505.00	44400.00
Repaired 2	280.60	6413.00	42900.00
Repaired 3	273.65	6157.00	45900.00
Repaired 4	261.43	6908.00	39000.00
Average	278.46	6495.75	43050.00
SD	15.33	311.79	2964.79
Average ± SD	278.46 ± 15.33	6495.75 ± 311.79	43050 ± 2964.79
Repaired Laminates-Manufacturing Method B			
Repaired 1	307.98	6355.00	42000.00
Repaired 2	285.17	7015.00	41900.00
Repaired 3	269.90	6054.00	40400.00
Repaired 4	293.24	6530.00	43000.00
Average	289.07	6488.50	41825.00
SD	15.89	402.30	1071.99
Average ± SD	289.07 ± 15.89	6488.5 ± 402.30	41825 ± 1071.99

[a] Obtained using 80 mm apart white dots via INSTRON AVE2 video extensometer.

stiffness compared to the repaired coupons. This indicates a more consistent quality in the pristine coupons compared to the repaired ones.

4.1.2. Stress-strain response

Fig. 17 presents stress-strain graphs for pristine, repair A, and repair B coupons, with characteristic information summarised in Table 7 and normalised comparisons shown in Fig. 18. The average slope of the stress-strain curve for pristine coupons (homogenised Young's modulus) is 46050 *MPa.* The homogenised Young's modulus of repairs A and B are 93% and 90% of the pristine coupons, respectively. Additionally, the repaired coupons achieve approximately 77% of the average strain of the pristine coupons, while the failure stress for repairs A and B is approximately 73% and 77% of the failure stress in the pristine coupons, respectively.

4.1.3. Failure mode

Fig. 19 displays filtered images indicating the points of damage initiation (red spots), failure path (yellow line for Repair A and orange line for Repair B), and endpoints of the failure path (blue spots) for three coupons of both Repair A and Repair B. It is important to note that the image filtration is a manual post-processing step to improve the visual presentation of the initiation and endpoints of the failure path. At load levels just before failure, the repair patch detaches from the parent laminate. As shown in the figure, this detachment is immediately followed by the failure of the specimen along fracture lines within the parent laminate.

Fig. 20 provides a macroscopic illustration of the failure damage for repairs A (left) and B (right). In both repairs, cohesive failure is observed in the overlap area of the $\pm 45_3$ parent ply group. However, in repair A (unlike repair B), there is evidence of cohesive damage in the $0/90_3$ overlap of the parent laminate, as shown in Fig. 20 (left). This damage is more pronounced at the edges of the ply group, where both peel and shear stresses are elevated. Thus, it can be inferred that the cohesive failure of the adhesive contributes to the detachment of the repair patch from the parent laminate. The failure of the $0/90_3$ and the $\pm 45_3$ plies at the bottom surface of the parent laminate aligns with the fibre orientation. In other words, the fracture of the $0/90_3$ and the $\pm 45_3$ ply groups occur at 90° and 45° to the tensile loading direction, respectively.

4.2. Numerical results

To interpret the experimental results, the 3D FEM of section 3.2.2 is first validated and then utilised to gain detailed understanding of the failure path and mechanism. This is particularly important, as CFRP
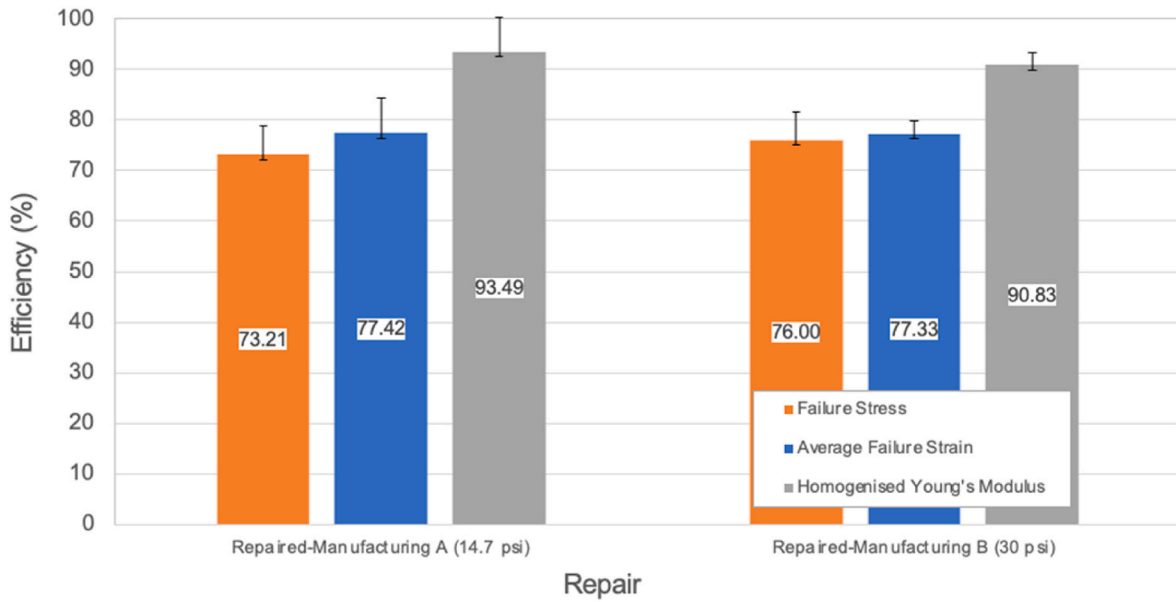
Fig. 18. The efficiency of repaired laminates, i.e. failure stress, failure axial strain and homogenised Young's modulus, normalised to pristine values for both manufacturing types A and B. The percentage ratio of the standard deviation to the mean values for each case is represented as bars ($100 \times SD/Mean$).
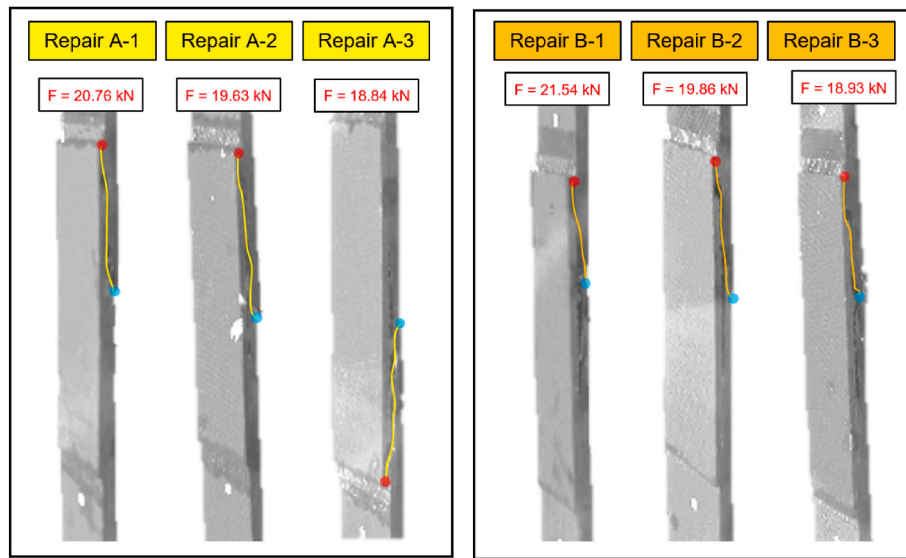
Fig. 19. Fracture path and failure mode of coupons 1–3 for repairs A (left) and B (right) shown on filtered image of coupons (red spots are damage initiation points and blue spots represent the end of failure path. Yellow/orange line is the fracture path. Top of the image is close to the loaded end and bottom is close to the fixed end).

structures often fail in a brittle and sudden manner, limiting the ability to study failure progression in experiments. The numerical model is validated against the experimental stress-strain curves of Repair B rather than force-displacement curves, due to potential compliance issues in the test apparatus. It should be noted that the experimental strain is the average axial strain measured by tracking the relative movement of two white dots on the back of the repaired coupons, spaced 80 mm apart, as shown in Fig. 14 (left).

The stress-strain graph for four experimental specimens and the FEA are shown in Fig. 21. It is clear from the graph that the FEA accurately replicates the laminate's homogenised stiffness, indicated by the slope of the stress-strain curve. Additionally, the FEA predicts a failure stress of 269.16 MPa, corresponding to a failure load of 18.81 kN. These values align closely with the average experimental results of 278.56 MPa and 19.35 kN for failure stress and load, respectively.

Fig. 22 shows the *x*-direction stresses for both the parent structure and the repair patch (top and bottom views) at various load levels. The stress distribution indicates that at load levels below final failure, i.e. 14 kN and 15 kN, the load path transitions from the parent structure into the repair patch and back into the parent structure (see Fig. 22a and b). However, at the failure load of 18.81 kN, the load path is confined to the parent structure. This indicates that the repair patch becomes ineffective due to adhesive failure (i.e. cohesive failure of the bond line) towards the loaded end, causing the stresses within the repair patch to approach zero (see Fig. 22c-2 and c-3).

Fig. 23 presents the overall scalar damage variable for cohesive elements (SDEG) in both the adhesive (Fig. 23a) and at delamination sites (Fig. 23b and c) at load levels of 14 kN, 15 kN and 18.81 kN. At 14 kN, damage within the adhesive initiates at the overlap edges, particularly in the $\pm 45°$ plies (see Fig. 23a–1). As the load increases to 15 kN, the
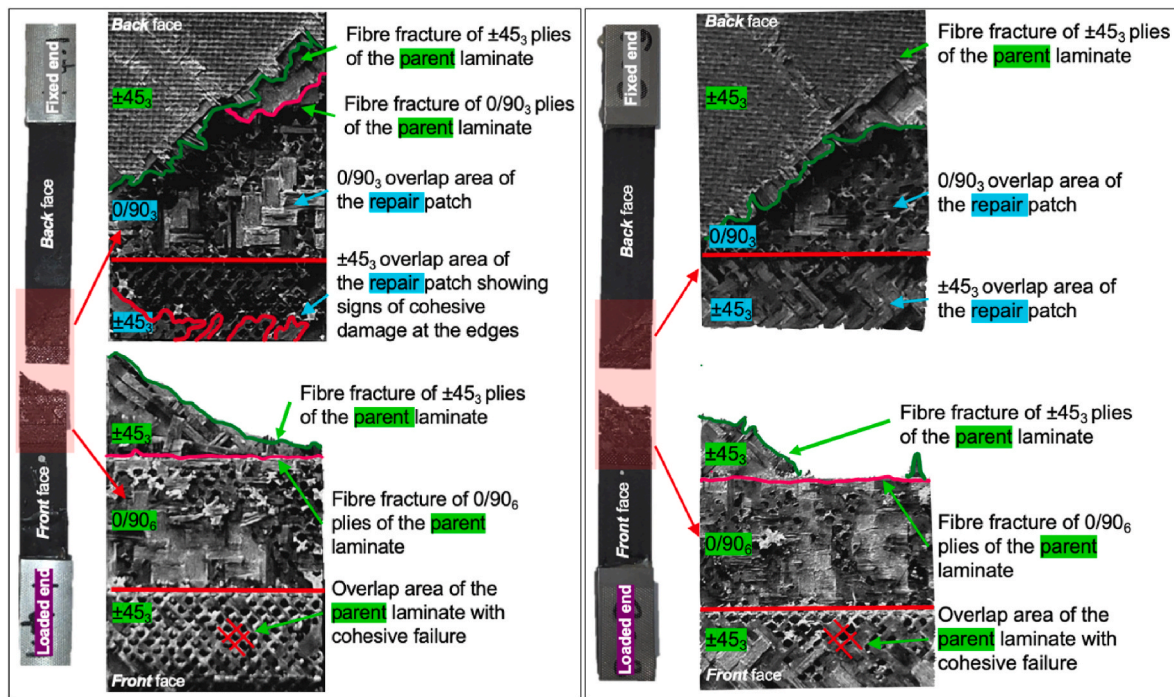
Fig. 20. Macroscopic illustration of failure for specimens of repair A (left) and repair B (right).
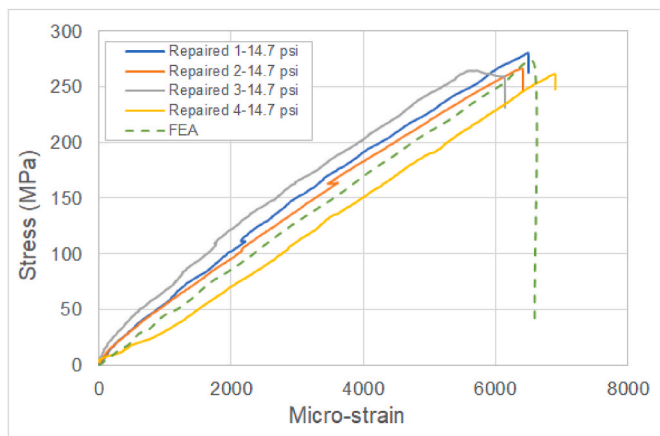
Fig. 21. Stress-strain graphs of experimental coupons (4 specimens) against FEA.

fracture energy increases, leading to further widespread adhesive damage (see Fig. 23b–1) until, at the failure load of 18.81 *kN*, most of the adhesive near the loaded end fails completely (Fig. 23c–1). This leads to the detachment of the repair patch from the parent laminate. It is important to note that, based on Fig. 23b and c, no delamination is expected within the repair patch throughout the loading process, as observed in the experiment. As in the experimental results, adhesive detachment is sudden and instantaneous.

Fig. 24 shows the STATUS variable for continuum elements of the repaired structure at failure, corresponding to a load of 18.81 *kN*.

A STATUS value of 1.0 indicates an active element, while 0.0 indicates a failed element. The figure shows that once the adhesive has completely failed, rendering the repair patch ineffective, the load path is redistributed into the parent laminate. This redistribution leads to overload and immediate failure at locations of high-stress concentration, specifically at a ply termination in the parent laminate $0/90_3^\circ$. This behaviour mirrors the experimental observations, where the structure

fails immediately after adhesive failure and repair patch detachment.

5. Conclusions

This study successfully implemented and validated a Variable Length Stepped Scarf (VLSS) repair scheme for Carbon Fibre Reinforced Polymer (CFRP) structures using both fully nonlinear 2D and 3D Finite Element Analysis (FEA). By incorporating advanced Cohesive Zone Modelling (CZM) of the adhesive bond-line, delamination modelling, progressive damage analysis, and consideration of geometric non-linearities, the study provides a comprehensive numerical framework for designing optimal repairs. The experimental validation demonstrated that the repair efficiency reached approximately $76 - 80\%$ of the original static strength, with higher recovery for Method B due to improved curing pressure.

The study highlights several key findings.

- **Repair Size Optimisation:** The optimisation of the step-lap length ratio played a crucial role in enhancing the performance of the VLSS repair scheme, demonstrating the effectiveness of a tailored approach in achieving a compact yet robust repair design.
- **Failure Mode:** Cohesive failure in the adhesive bond-line, particularly near the overlap edges, was the primary failure mechanism, as confirmed by both FEA and experimental results. This consistent failure mode across different tests underscores the need for further adhesive optimisation to mitigate early detachment of the repair patch.
- **Repair Efficiency:** The repair achieved a notable 14% improvement in static strength compared to previous studies, attributed to the optimised manufacturing techniques, such as the use of glass beads to maintain a uniform bond-line and increased curing pressure. Despite these improvements, the repair still did not restore full static strength, highlighting the challenge of bonded repairs for high-stress structures like aerospace components.
- **FEA Validation:** The agreement between the 3D FEA results and experimental data in terms of failure mode and load displacement confirms the robustness of the numerical models used in this study.
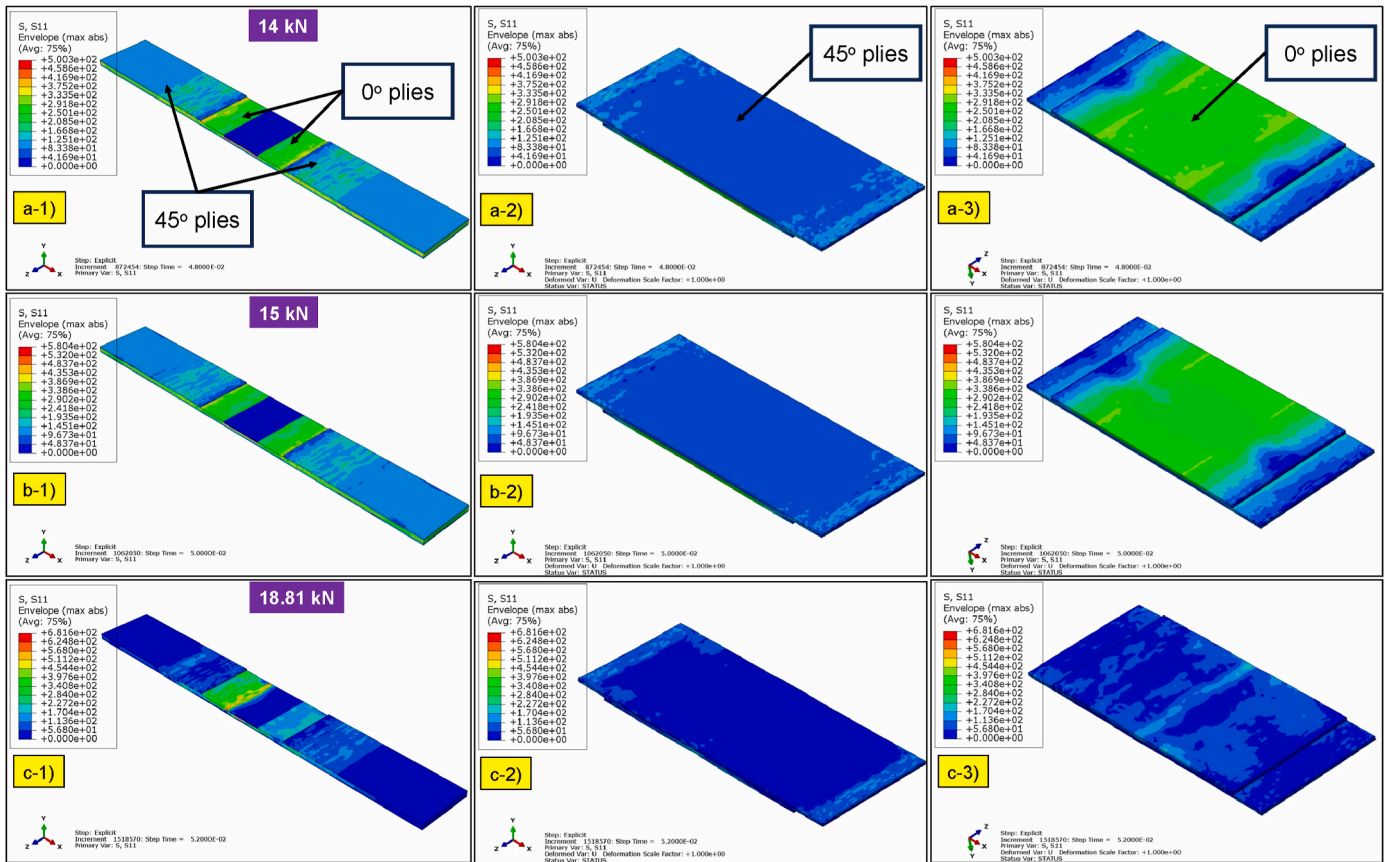
Fig. 22. Stress in *x*-direction for a) parent laminate, b) repair patch (top view) and c) repair patch (bottom view) at load levels 14 *kN*, 15 *kN* and 18.81 *kN*, respectively.

This provides a reliable foundation for future repair optimisation efforts and scalability assessments.

- **Manufacturing Methods**: The study highlighted the significance of manufacturing techniques, with Method B (higher curing pressure) showing slightly better repair performance. This underscores the importance of precision in manufacturing bonded repairs to enhance structural integrity.

6. Future work

Future studies should include.

- **Fatigue and Environmental Testing**: While this study focused on static tensile loading, future research should address the performance of the VLSS repair under fatigue loading conditions, which is critical for components in dynamic aerospace environments. Additionally, assessing the repair's long-term durability under environmental factors such as moisture, temperature variations, and UV exposure is crucial for ensuring real-world applicability.
- **Optimisation of Adhesive Properties**: The primary failure mode being cohesive adhesive failure suggests that further optimisation of adhesive material properties, such as improving toughness or exploring alternative adhesive formulations, is necessary to enhance repair strength and prevent premature detachment.
- **Scaling and Broader Applications**: Future research should explore the scalability of the VLSS repair method for larger composite structures, focusing on preserving repair efficiency while minimising repair size. Extending this approach to other load-bearing structures in aerospace and related industries could enhance repair strategies for composite materials. Additionally, the performance of this repair method should be evaluated under various loading conditions, such

as bi-axial compressive and tensile loads, to reflect more realistic scenarios.

- **Multi-Scale Modelling and Simulation:** Future studies could explore multi-scale modelling approaches to better understand the micro-mechanical behaviour of the repaired regions and predict failure initiation and progression at smaller scales. This can help refine the repair design and optimise material selection.
- **Advanced Non-Destructive Evaluation (NDE) Techniques:** Investigating and developing advanced non-destructive testing methods to accurately assess the integrity of the VLSS repair after application. This could include exploring ultrasonic testing, thermography, or digital image correlation techniques for identifying internal damage or delamination without compromising the structure.
- **Impact Resistance and Damage Tolerance:** Assessing the impact resistance and damage tolerance of the VLSS repair method is crucial for its application in high-risk environments like aerospace. Future studies could examine the repaired structure's response to low-velocity and high-velocity impacts to understand the effect of impact energy on repair integrity.
- **Cost-Effectiveness and Process Optimisation:** Evaluating the cost-effectiveness of the VLSS repair method in terms of material and manufacturing costs. Future research could focus on optimising the repair process to reduce costs and improve feasibility for large-scale applications in various industries.
- **Automated Repair Techniques:** Investigating the feasibility of using robotic systems or automated manufacturing processes to apply the VLSS repair method. This could improve precision, reduce labour costs, and minimise human error, leading to more consistent and reliable repairs.
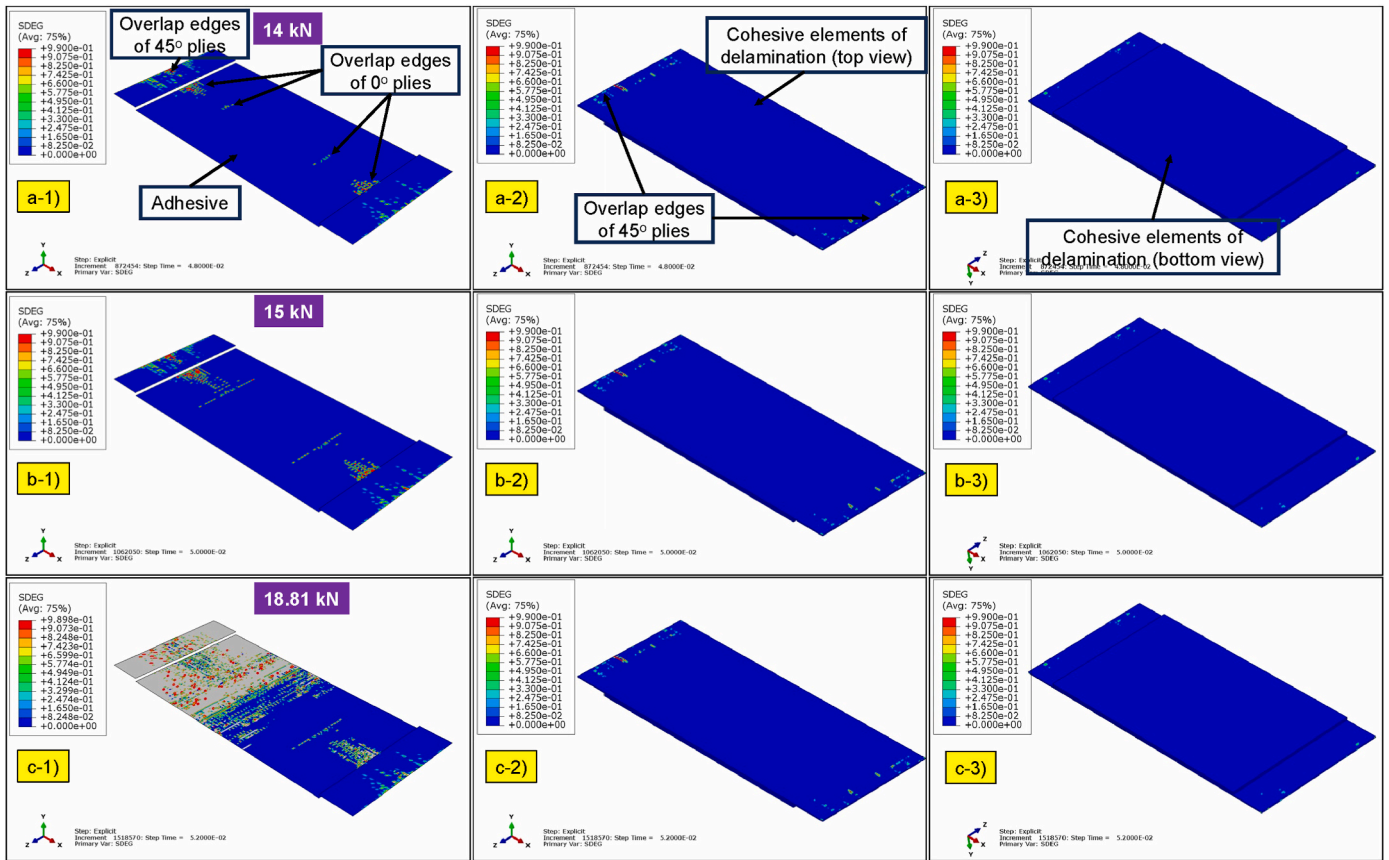
Fig. 23. Contour plot of SDEG parameter; a) parent laminate, b) repair patch (top view) and c) repair patch (bottom view) at load levels 14 *kN*, 15 *kN* and 18.81 *kN*, respectively (the grey scale shows the fully failed elements).
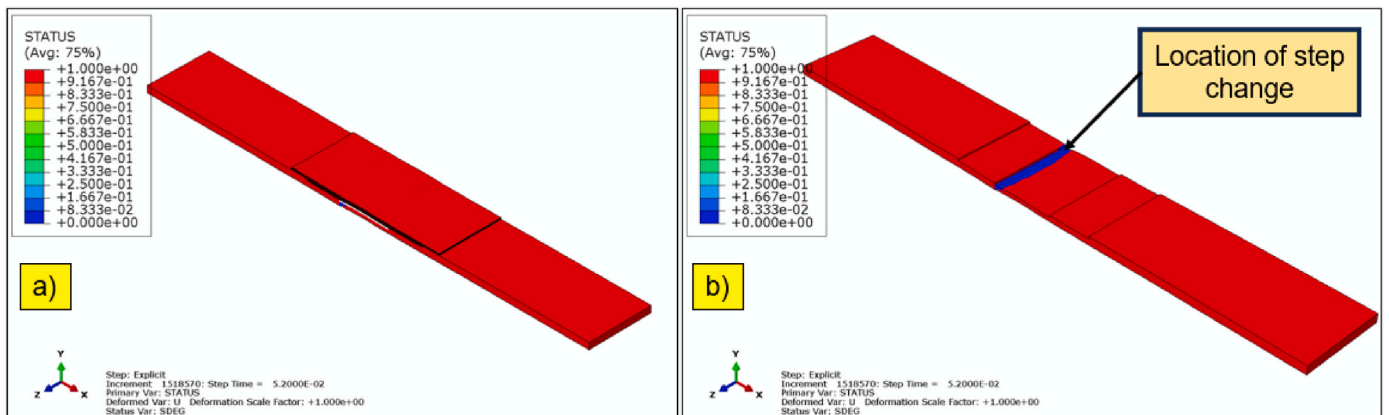
Fig. 24. Plot of STATUS variable for a) entire structure, b) parent structure at the time of maximum load, i.e. 18.81 *kN*.

CRediT authorship contribution statement

Mahdi Damghani: Writing – review & editing, Writing – original draft, Visualization, Validation, Supervision, Software, Resources, Project administration, Methodology, Investigation, Funding acquisition, Formal analysis, Data curation, Conceptualization. **George Egerton:** Investigation, Data curation. **Gary A. Atkinson:** Writing – review & editing, Investigation, Data curation. **Carwyn Ward:** Supervision,

Methodology. **Adrian Murphy:** Writing – review & editing.

Declaration of competing interest

The authors declare that they have no known competing financial interests or personal relationships that could have appeared to influence the work reported in this paper.

Appendix

The result of mesh sensitivity study for 3D FEM is shown in Figure A1.
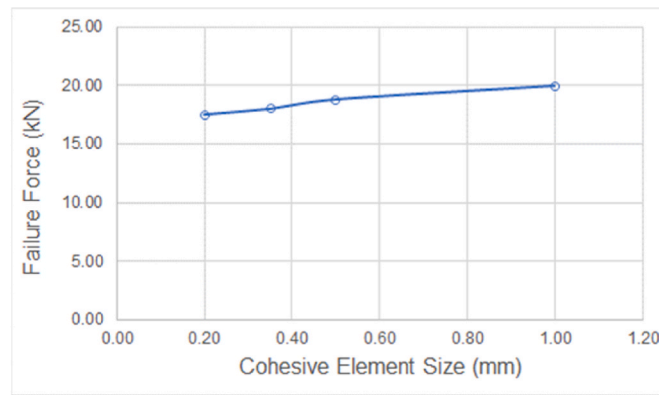
Fig. A1. Relationship between the size of cohesive elements and failure load of the optimum repair in 3D FEM.

The damage parameters used for the materials of study are obtained via experimental testing by the authors and are shown in Table A1.

Table A1
Damage parameters for the materials of study

Parameter	Unit	Description	Value	
			AX 5180 $0/90°$ **ply**	AX 5180 $\pm 45°$ **ply**
E_{1+}	MPa	Young's modulus along fibre direction 1 when $tr(\varepsilon) \geq 0$	63500.00	18000.00
E_{2+}	MPa	Young's modulus along fibre direction 2 when $tr(\varepsilon) \geq 0$	63500.00	18000.00
ϑ_{12+}	–	Poisson's ratio when $tr(\varepsilon) \geq 0$	0.30	0.30
G_{12}	MPa	Shear modulus	4831.00	4954.60
E_{1-}	MPa	Young's modulus along fibre direction 1 when $tr(\varepsilon) < 0$	63500.00	18000.00
E_{2-}	MPa	Young's modulus along fibre direction 2 when $tr(\varepsilon) < 0$	63500.00	18000.00
ϑ_{12-}	–	Poisson's ratio when $tr(\varepsilon) < 0$	0.30	0.30
X_{1+}	MPa	Tensile strength along fibre direction 1	620.00	220.00
X_{1-}	MPa	Compressive strength along fibre direction 1	403.00	220.00
X_{2+}	MPa	Tensile strength along fibre direction 2	620.00	220.00
X_{2-}	MPa	Compressive strength along fibre direction 2	403.00	220.00
S	MPa	Shear stress at the onset of shear damage	39.62	39.62
G_f^{1+}	N.mm/mm^2	Energy per unit area for tensile fracture along fibre direction 1	8.00	2.80
G_f^{1-}	N.mm/mm^2	Energy per unit area for compressive fracture along fibre direction 1	6.50	2.20
G_f^{2+}	N.mm/mm^2	Energy per unit area for tensile fracture along fibre direction 2	10.00	10.00
G_f^{2-}	N.mm/mm^2	Energy per unit area for compressive fracture along fibre direction 2	10.00	10.00
α_{12}	–	Parameter in the equation of shear damage	0.38	0.38
d_{12}^{max}	–	Maximum shear damage	0.67	0.67
$\overline{\sigma}_{0y}$	MPa	Initial effective shear yield stress	45.00	45.00
C	–	Coefficient in hardening equation	1326.42	1326.42
p	–	Power term in hardening equation	0.48	0.48

* $tr(\varepsilon) = \varepsilon_{11} + \varepsilon_{22}$.

**Determined for element characteristic length of 0.3 mm based on $G_f^{1+} = L_c g_0^{1+}$.

Data availability

Data will be made available on request.

References

[1] Damghani M, Ersoy N, Piorkowski M, Murphy A. Experimental evaluation of residual tensile strength of hybrid composite aerospace materials after low velocity impact. Compos B Eng 2019;179:107537.

[2] Fotouhi S, Khayatzadeh S, Pui Xia W, Damghani M, Bodaghi M, Fotouhi M. Detection of barely visible impact damage in polymeric laminated composites using a biomimetic tactile whisker. Polymers 2021;20:3587. https://doi.org/10.3390/polym13203587.

[3] Damghani M, Bolanos S, Chahar A, Matthews J, Atkinson GA, Murphy A, et al. Design, novel quality check and experimental test of an original variable length stepped scarf repair scheme. Compos B Eng 2022;230:109542. https://doi.org/10.1016/J.COMPOSITESB.2021.109542.

[4] Damghani M, Harrison C, Kennedy D. The effects of composite laminate stiffness and loading on stress resultant concentration factor around a hole. Proc Inst Mech Eng C J Mech Eng Sci 2018;232:0954406218755187. https://doi.org/10.1177/0954406218755187.

[5] Liu B, Xu F, Feng W, Yan R, Xie W. Experiment and design methods of composite scarf repair for primary-load bearing structures. Composites Part A Appl Sci Manuf 2016;88:27–38. https://doi.org/10.1016/j.compositesa.2016.05.011.

[6] Liu Y, Liu B. Elastic/plastic semi-analytical method for arbitrary curved surfaces of scarf repaired composites. In: 34th Congress of the international council of the aeronautical sciences. Florence: ICAS; 2024.

[7] Ridha M, Tan VBC, Tay TE. Traction–separation laws for progressive failure of bonded scarf repair of composite panel. Compos Struct 2011;93:1239–45. https://doi.org/10.1016/j.compstruct.2010.10.015.

[8] Bendemra H, Compston P, Crothers PJ. Optimisation study of tapered scarf and stepped-lap joints in composite repair patches. Compos Struct 2015;130:1–8. https://doi.org/10.1016/j.compstruct.2015.04.016.

[9] Han Q, Liu B, Xie W. The tension failure mechanisms of composite stepped bonding repairs and joints for the aircraft primary load-bearing structures. J Adhes Sci Technol 2019;33:675–90. https://doi.org/10.1080/01694243.2018.1558477.

[10] Psarras S, Loutas T, Galanopoulos G, Karamadoukis G, Sotiriadis G, Kostopoulos V. Evaluating experimentally and numerically different scarf-repair methodologies of composite structures. Int J Adhesion Adhes 2020;97:102495. https://doi.org/10.1016/j.ijadhadh.2019.102495.

[11] Breitzman TD, Iarve EV, Cook BM, Schoeppner GA, Lipton RP. Optimization of a composite scarf repair patch under tensile loading. Composites Part A Appl Sci Manuf 2009;40:1921–30. https://doi.org/10.1016/j.compositesa.2009.04.033.

[12] Pinto AMGG, Campilho RDS, De Moura MFS, Mendes IR. Numerical evaluation of three-dimensional scarf repairs in carbon-epoxy structures. Int J Adhesion Adhes 2010;30:329–37. https://doi.org/10.1016/j.ijadhadh.2009.11.001.

[13] Goh JY, Georgiadis S, Orifici AC, Wang CH. Effects of bondline flaws on the damage tolerance of composite scarf joints. Composites Part A Appl Sci Manuf 2013;55:110–9. https://doi.org/10.1016/j.compositesa.2013.07.017.

[14] Orsatelli J-B, Paroissien E, Lachaud F, Schwartz S. Bonded flush repairs for aerospace composite structures: a review on modelling strategies and application to repairs optimization, reliability and durability. Compos Struct 2023;304:116338. https://doi.org/10.1016/j.compstruct.2022.116338.

[15] Li H, Chen C, Wang T, Wang L. Experimental study of stepped-lap scarf joint repair for spar cap damage of wind turbine blade in Service. Appl Sci 2020;10. https://doi.org/10.3390/app10030922.

[16] Niedernhuber M, Holtmannspötter J, Ehrlich I. Fiber-oriented repair geometries for composite materials. Compos B Eng 2016;94:327–37. https://doi.org/10.1016/j.compositesb.2016.03.027.

[17] Wang S, Xie Z, Li X. On adhesively bonded stepped-scarf joint: an analytical model and its validation. Mech Adv Mater Struct 2021;28:938–51. https://doi.org/10.1080/15376494.2019.1614699.

[18] Masmanidis IT, Philippidis TP. Modeling the progressive failure of scarf joints for wind turbine blade repair. J Compos Mater 2017;52:2243–54. https://doi.org/10.1177/0021998317740731.

[19] Ghazali E, Dano M-LL, Gakwaya A, Amyot C-OO. Experimental and numerical studies of stepped-scarf circular repairs in composite sandwich panels. Int J Adhesion Adhes 2018;82:41–9. https://doi.org/10.1016/j.ijadhadh.2017.12.008.

[20] Sun L, Tie Y, Hou Y, Lu X, Li C. Prediction of failure behavior of adhesively bonded CFRP scarf joints using a cohesive zone model. Eng Fract Mech 2020;228:106897. https://doi.org/10.1016/j.engfracmech.2020.106897.

[21] Wu C, Chen C, He L, Yan W. Comparison on damage tolerance of scarf and stepped-lap bonded composite joints under quasi-static loading. Compos B Eng 2018;155:19–30. https://doi.org/10.1016/j.compositesb.2018.08.031.

[22] Han Q, Liu B, Xie W. The tension failure mechanisms of composite stepped bonding repairs and joints for the aircraft primary load-bearing structures. J Adhes Sci Technol 2019;33:675–90. https://doi.org/10.1080/01694243.2018.1558477.

[23] Damghani M, Wallis C, Bakunowicz J, Murphy A. Using laminate hybridisation (CFRP-GFRP) and shaped CFRP plies to increase plate post-buckling strain to failure under shear loading. Thin-Walled Struct 2021;162:107543. https://doi.org/10.1016/j.tws.2021.107543.

[24] Woo K. Fracture analysis of woven textile composite using cohesive zone modeling. J Mech Sci Technol 2017;31:1629–37. https://doi.org/10.1007/s12206-017-0310-2.

[25] Turon A, Dávila CG, Camanho PP, Costa J. An engineering solution for mesh size effects in the simulation of delamination using cohesive zone models. Eng Fract Mech 2007;74:1665–82. https://doi.org/10.1016/j.engfracmech.2006.08.025.

[26] Costa M, Viana G, Créac'hcadec R, da Silva LFM, Campilho RDSG. A cohesive zone element for mode I modelling of adhesives degraded by humidity and fatigue. Int J Fatig 2018;112:173–82. https://doi.org/10.1016/j.ijfatigue.2018.03.014.

[27] Abaqus. 2017.

[28] Damghani M, Pir RA, Murphy A, Fotouhi M. Experimental and numerical study of hybrid (CFRP-GFRP) composite laminates containing circular cut-outs under shear loading. Thin-Walled Struct 2022;179:109752. https://doi.org/10.1016/j.tws.2022.109752.

[29] Lisle T, Bouvet C, Pastor ML, Rouault T, Marguerès P. Damage of woven composite under tensile and shear stress using infrared thermography and micrographic cuts. J Mater Sci 2015;50:6154–70. https://doi.org/10.1007/s10853-015-9173-z.

[30] Chen C, Sun C, Han X, Hu D, Zhou J, Guan Z. The structural response of the thermoplastic composite joint subjected to out-of-plane loading. Int J Impact Eng 2020;145:103691. https://doi.org/10.1016/J.IJIMPENG.2020.103691.

[31] Sitnikova E, Guan ZW, Cantwell WJ. The analysis of the ultimate blast failure modes in fibre metal laminates. Compos Sci Technol 2016;135:1–12. https://doi.org/10.1016/J.COMPSCITECH.2016.09.006.

[32] Truong V-H, Kwak B-S, Roy R, Kweon J-H. Cohesive zone method for failure analysis of scarf patch-repaired composite laminates under bending load. Compos Struct 2019;222:110895. https://doi.org/10.1016/j.compstruct.2019.110895.

[33] Liu Z, Xia Y. Development of a numerical material model for axial crushing mechanical characterization of woven CFRP composites. Compos Struct 2019;230:111531. https://doi.org/10.1016/j.compstruct.2019.111531.

[34] Liu H, Falzon BG, Dear JP. An experimental and numerical study on the crush behaviour of hybrid unidirectional/woven carbon-fibre reinforced composite laminates. Int J Mech Sci 2019;164:105160. https://doi.org/10.1016/j.ijmecsci.2019.105160.

[35] Yan H, Oskay C, Krishnan A, Xu LR. Compression-after-impact response of woven fiber-reinforced composites. Compos Sci Technol 2010;70:2128–36. https://doi.org/10.1016/j.compscitech.2010.08.012.

[36] Santos JPJR, Marques EAS, Carbas RJC, Gilbert F, da Silva LFM. Experimental study of the impact of glass beads on adhesive joint strength and its failure mechanism. Materials 2021;14. https://doi.org/10.3390/ma14227013.

[37] Damghani M, Saddler J, Sammon E, Atkinson GA, Matthews J, Murphy A. An experimental investigation of the impact response and Post-impact shear buckling behaviour of hybrid composite laminates. Compos Struct 2023;305:116506. https://doi.org/10.1016/j.compstruct.2022.116506.